Mechanosensation of tight junctions by ZO-1 phase separation and flow

Cornelia Schwayer[1], Shayan Shamipour[1], Kornelija Pranjic-Ferscha[1], Alexandra Schauer[1], Maria Balda[3], Masazumi Tada[2], Karl Matter[3] and Carl-Philipp Heisenberg[1,4*]

[1] Institute of Science and Technology Austria, Klosterneuburg, Austria

[2] Department of Cell and Developmental Biology, University College London, London, UK

[3] Institute of Ophthalmology, University College London, London, UK

[4] Lead Contact

* Correspondence: heisenberg@ist.ac.at

Summary

Cell-cell junctions respond to mechanical forces by changing their organization and function. The molecular processes underlying this mechanosensitivity are still incompletely understood. Here we show that in the gastrulating zebrafish embryo, tight junction (TJ) mechanosensitivity is mediated by actomyosin-driven flow of phase-separated Zonula Occludens-1 (ZO-1) clusters. We found that ZO-1 junctional accumulation at the contact between the Enveloping Layer (EVL) and the Yolk Syncytial Layer (YSL) closely scales with actomyosin tension. Actomyosin tension triggers ZO-1 junctional accumulation by driving retrograde actomyosin flow within the YSL that transport non-junctional ZO-1 clusters towards the TJ. Non-junctional ZO-1 clusters form by phase separation, and direct binding of ZO-1 to actin is required for stable incorporation of ZO-1 clusters into TJ. If the formation and/or junctional incorporation of ZO-1 clusters is impaired, TJ lose their mechanosensitivity, and, consequently, EVL-YSL movement is delayed. Thus, phase separation and flow of non-junctional ZO-1 confer mechanosensitivity to TJ.

Introduction

A key step in the emergence of multicellularity is the development of different junctional complexes mechanically connecting cells and allowing the transfer of biochemical and mechanical signals between cells. The molecular composition and dynamic regulation of different cell-cell junction types, such as adherens junctions (AJ), tight junctions (TJ) and desmosomes, have been extensively studied over the past decades (Van Itallie and Anderson 2014; Franke 2009; Godsel et al. 2004; Niessen 2007). Likewise, detailed insight has been gained in the intracellular signaling cascades activated by the different junctional complexes and their function in tissue homeostasis (Matter and Balda 2003; Wheelock and Johnson 2003; Johnson, Najor, and Green 2014; Zihni et al. 2016). There is also compelling evidence that changes in the molecular composition, size and turnover of junctional complexes directly affect both their mechanical integrity and signaling activity (Baum and Georgiou 2011; Shen, Weber, and Turner 2008; Cunningham and Turner 2012; Nekrasova and Green 2013). In contrast, much less is known about how mechanical forces influence cell-cell junction formation and signaling.

Recent studies on AJ indicate that mechanical forces and actin dynamics at E-cadherin-mediated cell-cell contacts can promote E-cadherin clustering, leading to the formation of larger and more stable junctional complexes (Engl et al. 2014; Ladoux et al. 2010; M. Cavey and Lecuit 2009; Matthieu Cavey et al. 2008). An important step in this mechanosensing process is the modulation of AJ anchoring to the cortical actomyosin network, with junctional tension changing the conformation of AJ components, such as α-catenin and vinculin, thereby increasing their binding capacity to the

actomyosin network (Gomez, McLachlan, and Yap 2011; Watabe-Uchida et al. 1998; Weiss et al. 1998; Yonemura et al. 2010). Tension-dependent changes in the composition and organization of AJ are thought to affect both their coupling strength and signaling activity (Gomez, McLachlan, and Yap 2011). While recent studies suggest that certain components of other junction types, such as TJ, can in principle undergo conformational changes upon mechanical loading (Spadaro et al. 2017), it is not yet entirely clear whether and how this molecular mechanosensitivity translates into changes of global junction organization and function.

TJ play an essential role in tissue homeostasis by limiting the passage of molecules and ions between cells and restricting the movement of molecules between the apical and basolateral domains thereby maintaining apicobasal polarity of epithelial cells (Shin, Fogg, and Margolis 2006). Similar to AJ, TJ are composed of transmembrane proteins, such as Occludins and Claudins, and cytoplasmic scaffolding proteins connecting the transmembrane proteins to the cytoskeleton, e.g. Zonula Occludens (ZO) proteins and Cingulins (Zihni et al. 2016). TJ also function as intracellular signaling centers regulating the activity of small Rho GTPases, such as RhoA and Cdc42, thereby affecting actomyosin network organization and contraction at the junction (Zihni and Terry, 2015). Conversely, actomyosin regulators such as RhoA, Cdc42 and Rac have been shown to be important for TJ formation (Zihni et al., 2016); yet, to what extent mechanical signals, for instance by triggering conformational changes of TJ components (Spadaro et al., 2017), are involved in this process still needs to be demonstrated.

During zebrafish epiboly, the enveloping cell layer (EVL), a simple squamous epithelial monolayer covering the blastoderm at the animal pole of the yolk cell, spreads together with the underlying deep cells over the entire yolk cell (Figure 1A) (Lepage and Bruce 2010; Bruce 2016). EVL spreading is driven by a large actomyosin ring-like structure positioned within the yolk syncytial layer (YSL) on the surface of the yolk cell and presumably coupled to the EVL leading edge by TJ (Figure 1A) (Behrndt et al. 2012; Holloway et al. 2009; Köppen et al. 2006; Cheng, Miller, and Webb 2004). The actomyosin ring drives EVL spreading by actively pulling on the EVL-leading edge through two distinct motor-activities: (i) a cable-constriction motor, where the actomyosin band constricts around its circumference, thereby generating pulling forces on the EVL margin once the band has crossed the yolk cell equator; and (ii) a flow-friction motor, where a gradient of actomyosin tension along the width of the actomyosin band gives rise to retrograde actomyosin flow (Behrndt et al. 2012). This actomyosin flow, when resisted by friction to adjacent structures within the YSL, will generate a traction force pulling the EVL margin towards the vegetal pole (Behrndt et al. 2012). The pulling forces generated by the actomyosin band within the YSL are likely transmitted to the margin of the EVL by junctional complexes connecting the leading edge of the EVL to the YSL (Behrndt et al. 2012; Köppen et al. 2006). Whether and how junction formation at the EVL-YSL boundary relates to actomyosin ring formation and function within the YSL is still unknown.

Here, we show that TJ rather than AJ components accumulate at the EVL-YSL boundary during the course of EVL epiboly, and that this accumulation closely scales with the degree of actomyosin tension within the YSL. We further show that the accumulation of TJ components at the EVL-YSL boundary is mediated by tension-dependent retrograde actomyosin flow within the YSL transporting non-junctional phase-separated ZO-1b clusters towards the boundary. Finally, we show that the junctional incorporation of those clusters depends on ZO-1b binding to actin, and that the mechanosensitive response of TJ at the EVL-YSL junction is required for proper EVL spreading.

Results

Tight junction components accumulate at the EVL-YSL boundary

We have previously noted that both AJ and TJ components localize to the boundaries between EVL cells and at the leading edge of the EVL where it contacts the YSL (Köppen et al. 2006). To investigate which junctions form at the EVL-YSL boundary during the course of EVL epiboly, we systematically analyzed how the localization of various AJ and TJ components changes. Interestingly, we found that the accumulation of components typically associated with AJ, such as E-cadherin, α-catenin and β-catenin, decreased at the EVL-YSL boundary during epiboly (Figures 1A-D and S1A-D). In contrast, the accumulation of various components typically associated with TJ either increased (ZO-1b, Cingulin-like 1) or remained unchanged (ZO-3, Claudin-D and Occludin-A) at this boundary during epiboly (Figures 1A-D and S1A-D). This suggests that during the course of EVL epiboly, TJ becomes the predominant junction type connecting the EVL leading edge to the YSL.

ZO-1b and ZO-3 are required for proper EVL epiboly movements by regulating actomyosin flow and tension within the YSL

To determine whether this accumulation of TJ components at the EVL-YSL boundary during epiboly is functionally relevant for EVL epiboly movements, we sought to interfere with the expression of those components and analyze resultant changes in EVL epiboly movements. Given the known signaling function of TJ in regulating actin network organization and contraction (Zihni and Terry 2015), we speculated that TJ might function in EVL epiboly movements by controlling actomyosin ring formation and flow within the YSL, previously shown to drive EVL epiboly movements (Behrndt et al. 2012). To test this possibility, we injected *morpholinos* (MO) directed against the TJ components *zo-1b* and *zo-3,* previously implicated in TJ organization and signaling to the actomyosin cytoskeleton (Itoh et al. 2012; Otani et al. 2006; Tornavaca et al. 2015; Wittchen, Haskins, and Stevenson 2003), directly into the YSL to specifically interfere with ZO-1b/3 expression at the EVL-YSL boundary (Figure 2A). YSL morphant embryos displayed clearly reduced EVL epiboly movements, which could be partially rescued by co-injecting GFP-tagged *zo-1b and zo-3* mRNA (Figure 2A-A'', Video S1). In contrast, injection of *zo-1b* and *zo-3* mismatch MOs or a standard negative control MO into the YSL did not elicit a recognizable epiboly phenotype (Figure S2A), supporting the specificity of the *zo-1b/3* MO effect. Slower EVL spreading was accompanied by diminished retrograde actomyosin flow and ring formation within the YSL (Figure 2C-C',D-D', Video S2), a phenotype that could be partially rescued by co-injecting GFP-tagged *zo-1b and zo-3* mRNA (Figures 2C-C',D-D', Video S2). Notably, the epiboly phenotype in *zo-1b/3* morphant embryos was not due to a general developmental delay, as YSL morphant embryos formed the first somite, visualized by *papc* expression, at the same time as their control injected siblings (Figure S2B-B'). Together, these observations suggest that TJ formation at the EVL-YSL boundary is required for EVL epiboly movements by regulating actomyosin flow and ring formation within the YSL.

To determine whether the obtained morphant phenotypes were specific, we generated maternal-zygotic (MZ) mutants for the TJ components ZO-1b and ZO-3, using CRISPR/Cas9 technique (Figure S2C). We found that in MZ*zo-1b* and MZ*zo-3* single mutants, EVL spreading appeared largely unaffected (Figure S2D). Interestingly, MZ*zo-1b/3* double mutants displayed a phenotype closely resembling the phenotypes observed in embryos where ZO-1b and ZO-3 expression was knocked down either uniformly or locally within the YSL using MOs (Figures 2B-B'', A-A'' and S2G''). The phenotypic similarities between mutant and morphant embryos further suggest that the obtained *zo-1b/3* morphant phenotypes were specific and, thus, that the *zo-1b* and *zo-3* MOs can be used to analyze the function of those proteins in EVL-YSL epiboly. Additionally, when *zo-1b/3* was ubiquitously knocked down or knocked out (MZ*zo-1b/3* mutants), the majority of morphant or mutant embryos formed the first somite on time (Figure S2E-E'), suggesting that the observed epiboly phenotype is not due to a general delay in the development of mutant or morphant embryos. Notably, TJ were reduced but not completely absent at the EVL-YSL boundary in *zo-1b/3* YSL morphants (Figure S2F-F') and mutants (Figure S2G-G'), likely due to incomplete knockdown in

morphant embryos and functional redundancy and/or compensatory upregulation in the expression of the remaining *zo* genes (*zo-1a, zo-2a, zo-2b*) in mutant embryos (Figure S2H).

It has previously been shown that gradients of actomyosin contractility can trigger actin flows (Mayer et al. 2010; Munro, Nance, and Priess 2004; Lecuit, Lenne, and Munro 2011). Hence, we asked whether TJ components control actomyosin flow within the YSL by modulating tension at the EVL-YSL boundary. To address this possibility, we measured tension at the EVL-YSL boundary oriented along the circumference of the yolk cell in wild type and *zo-1b/3* YSL morphant embryos using UV-laser ablation. We found that junctional tension was strongly reduced in *zo-1b/3* YSL morphants compared to wild type embryos at late stages of epiboly (8 hpf; Figures 2E-E'' and S2I-I'). Together, these data indicate that normal TJ formation is required for proper buildup of tension at the EVL-YSL boundary and, consequently, actomyosin flow within the YSL, which is required for proper EVL epiboly movements.

Actomyosin contractility controls ZO-1 recruitment to the EVL-YSL boundary

Our junctional tension measurements at the EVL-YSL boundary in wild type embryos also revealed that tension was considerably higher at late (8 hpf) compared to early-mid (6 hpf) stages of epiboly (Figures 2F-F'' and S2J-J'), consistent with our previous observation that actomyosin network tension within the YSL increases during the course of epiboly (Behrndt et al. 2012). Interestingly, this increase of junctional tension coincides with TJ component accumulation at the EVL-YSL boundary (Figure 1A-D), pointing at the intriguing possibility that TJ might be mechanosensitive. To determine whether and how increased junctional tension at the EVL-YSL boundary relates to TJ formation at this interface, we sought to modulate actomyosin contractility within the YSL and determine resultant effects on TJ formation at the EVL-YSL boundary. To modulate actomyosin contractility specifically within the YSL, we performed YSL-injections of mRNAs encoding constitutive active (ca) versions of either Myosin Phosphatase (caMypt) (Smutny et al. 2017; Jayashankar et al. 2013) or RhoA (caRhoA) (Takesono et al. 2012), previously shown to decrease or increase actomyosin contractility, respectively. Strikingly, we found that in embryos with reduced actomyosin contractility and retrograde flow rates within the YSL (Figures S3A-A',B-B' and 2C-C',D-D' - ctrl), the accumulation of ZO-1b, at the EVL-YSL boundary was clearly reduced (Figure 3A-A''). Conversely, ZO-1b at the EVL-YSL boundary showed a premature and strong accumulation in embryos with increased actomyosin contractility and retrograde flow rates within the YSL (Figures 3B-B'' and S3C-C',D-D'). AJ components, in contrast, did not display any recognizable changes in response to altered actomyosin tension at the EVL-YSL junction (Figure S3E-E'). Collectively, these findings indicate that actomyosin network contractility and retrograde flow within the YSL triggers TJ component accumulation at the EVL-YSL boundary, suggesting that TJ at this boundary are mechanosensitive.

Non-junctional clusters of ZO-1b within the YSL form by phase separation, undergo retrograde flows and are incorporated into TJ at the EVL-YSL boundary

To understand how actomyosin network tension translates into the accumulation of TJ components at the EVL-YSL boundary, we performed high-resolution time-lapse imaging of ZO-1b accumulation at the EVL-YSL boundary at 7 hpf. Remarkably, in addition to junctional ZO-1b, we detected non-junctional clusters of ZO-1b within the YSL close to the EVL-YSL boundary, which traversed at a similar velocity as the actomyosin network towards this boundary (Figure 4A-A'',B-B'', Video S3). ZO-1b clusters arriving at the EVL-YSL boundary were then incorporated into the junction, thereby locally increasing the amount of ZO-1b at the junction (Figure 4C-C'). Closer analysis of these non-junctional ZO-1b clusters showed that ZO-1b close to the EVL-YSL boundary displayed a tendency to fuse into larger clusters (Figure 4D-D'', Video S4). Given that fusion of protein clusters or 'droplets' has previously been associated with protein phase separation (Brangwynne et al. 2009; P. Li et al.

2012), this points at the intriguing possibility that non-junctional ZO-1b clusters within the YSL might form by phase separation. To form phase-separated droplets, multivalent interactions on an intra- or inter-molecular level are necessary (P. Li et al. 2012; Kato et al. 2012; Banani et al. 2017). Indeed, ZO-1 can undergo multivalent interactions with other ZO proteins such as ZO-2 and ZO-3 as well as other TJ scaffolding proteins, such as Cingulins (Utepbergenov, Fanning, and Anderson 2006; A. S. Fanning et al. 1998). There is also evidence for intra-molecular interaction sites for ZO-1 and other members of the MAGUK (membrane-associated guanylate kinases) protein family (Ye, Zeng, and Zhang 2018; Lye et al. 2010; Spadaro et al. 2017; Alan S. Fanning et al. 2007). This suggests that ZO-1b might be capable of undergoing phase separation, and that this property might contribute to its previously demonstrated scaffolding function in recruiting other proteins to TJ (Bauer et al. 2010; Matter and Balda 2003; Alan S. Fanning and Anderson 2009).

To test whether ZO-1b within the YSL shows further properties indicative of a phase separation process, we sought to analyze ZO-1b turnover in clusters adjacent to the EVL margin using Fluorescence recovery after photobleaching (FRAP). Based on previous observations that proteins undergoing liquid-liquid phase separation stay highly dynamic within phase-separated droplets (Brangwynne et al. 2009; Hyman, Weber, and Jülicher 2014), we hypothesized that if ZO-1b would undergo phase separation within the YSL, then the turnover of the ZO-1b non-junctional pool should be rather fast. Consistent with ZO-1b potentially undergoing phase separation, we found that at early-mid gastrulation stages (5-6 hpf) non-junctional ZO-1b showed fast turnover on a second scale ($t_{1/2}$ fast = 4 sec) and almost all of it was mobile (99% mobile fraction) (Figure 4E-E''). Interestingly, non-junctional ZO-1b also exhibited turnover on a minute scale ($t_{1/2}$ slow = 140 sec) indicative of the presence of a second, slower ZO-1b species (Figure 4E-E''). Surprisingly, however, at later gastrulation stages (7-8 hpf), the turnover time of non-junctional ZO-1b during the fast phase ($t_{1/2}$ fast) increased (4 sec to 13 sec) and its mobile fraction decreased (from 99% to 64% mobile fraction) (Figure 4F-F''). This suggests that clusters of non-junctional ZO-1b within the YSL, initially displaying properties of liquid-liquid phase-separated condensates, might undergo a maturation process leading to their immobilization. Interestingly, analyzing turnover of ZO-1b directly at the EVL-YSL junction at early (5 hpf) and later stages of gastrulation (8 hpf) revealed an even smaller fraction (~40%) of mobile ZO-1b at both of these stages (Figure S4A-A'',B-B''), suggesting that junctional incorporation of ZO-1b might further promote its immobilization.

To further test whether non-junction ZO-1b clusters indeed form by phase separation, we analyzed its dependency on concentration, a typical feature of a thermodynamically driven phase separation processes. To determine how the concentration of ZO-1b expressed within the YSL relates to cluster formation of ZO-1b, we analyzed the size and fusion rate of those clusters as a function of ZO-1b concentration within the YSL. We found that both the size and fusion rate of non-junctional clusters of ZO-1b linearly scaled with the concentration of ZO-1b expressed within the YSL (Figures 5A-A''' and S5A), demonstrating that cluster formation is dependent on ZO-1b concentration as expected for a phase separation mechanism.

Different domains of ZO-1b have previously been associated with ZO proteins binding to each other (Utepbergenov, Fanning, and Anderson 2006; A. S. Fanning et al. 1998; Alan S. Fanning et al. 2007) and the actin cytoskeleton (Alan S. Fanning, Ma, and Anderson 2002; A. S. Fanning et al. 1998). To determine whether those multivalent interactions are important for ZO-1b cluster formation and presumed phase separation behavior, we generated deletion constructs lacking certain regions of ZO-1b and asked how this affects ZO-1b cluster formation. First, we tested a C-terminally truncated version of ZO-1b (ZO-1bΔC) (Figure 5B), which has recently been found in *in vitro* reconstitution and cell culture assays to be defective in undergoing phase separation likely due to changes in intra-molecular interactions of the truncated protein (Beutel et al., n.d.). Substituting full-length ZO-1b

with ZO-1bΔC by expressing ZO-1bΔC in Mz*zo-1b/3* mutant embryos revealed that ZO-1bΔC exclusively localized to TJ between EVL cells and at the EVL-YSL boundary and was unable to form non-junctional clusters within the YSL (Figure 5C). This is consistent with the notion that non-junctional ZO-1b clusters within the YSL might form by phase separation.

Since the C-terminus of ZO-1b also harbors an actin binding region (ABR) (Alan S. Fanning, Ma, and Anderson 2002) (Figure 5B) and non-junctional ZO-1b appears to partially co-localize with the cortical actomyosin network within the YSL (Figure S5B-B'), we further hypothesized that the failure of ZO-1bΔC in undergoing phase separation and forming non-junctional clusters within the YSL might also be caused by its inability to directly bind to actin. To test this possibility, we generated a version of ZO-1b specifically lacking its ABR (ZO-1bΔABR) and substituted full-length ZO-1b with ZO-1bΔABR in MZ*zo-1b/3* mutant embryos. Unexpectedly, we found that in ZO-1bΔABR expressing MZ*zo-1b/3* mutant embryos, non-junctional clusters still formed and underwent fusion similar to full-length ZO-1b (Figure 5D-D''). However, analysis of cluster size and shape in ZO-1bΔABR expressing embryos revealed that these clusters took more spherical droplet-like shapes compared to the elongated rod-like shapes typically observed when expressing full-length ZO-1b (Figure 5D'''-D''''). This points at the intriguing possibility that direct binding of ZO-1b to actin is not required for ZO-1b to undergo phase separation and to form non-junctional clusters within the YSL. Rather, actin binding might restrict the ability of ZO-1b to form more spherical droplet-like clusters within the YSL.

To determine whether an intact actomyosin network is required for ZO-1b phase separation and cluster formation, we disassembled the actomyosin network within the YSL by exposing embryos to Latrunculin B blocking actin polymerization. Strikingly, disassembly of the actomyosin network led to the formation of much larger and more spherical droplet-like clusters of non-junctional ZO-1b within the YSL than found in DMSO-exposed control embryos (Figure 5E-E''). Moreover, these clusters underwent fusion within the YSL despite the notable absence of actomyosin network structures between those clusters (Figures 5F and S5C-C', Video S5), suggesting that these clusters can fuse independently from actomyosin network contraction. Collectively, these findings indicate that ZO-1b forms non-junctional clusters within the YSL by phase separation, and that ZO-1b binding to actin gives ZO-1b clusters within the YSL their characteristic elongated rod-like shapes.

<u>TJ mechanosensitivity is mediated by retrograde actomyosin flows within the YSL transporting non-junctional phase-separated ZO-1b clusters towards the junction</u>

Next, we investigated whether ZO-1b phase separation is required for TJ mechanosensitivity at the EVL-YSL boundary. To this end we substituted full-length ZO-1b with ZO-1bΔC, incapable of forming phase-separated non-junctional clusters within the YSL (Figure 5C), by expressing ZO-1bΔC in MZ*zo-1b/3* mutant embryos. For monitoring TJ mechanosensitivity, we increased YSL actomyosin tension by expressing caRhoA within the YSL and analyzed how this affects junctional accumulation of ZO-1bΔC. We found that junctional ZO-1bΔC levels remained unchanged in response to caRhoA-mediated increased actomyosin tension and flow within the YSL (Figure 6B-B', A-A' - ctrl), suggesting that the ability of ZO-1b to form non-junctional phase-separated clusters within the YSL is critical for TJ mechanosensitivity. Importantly, the failure of ZO-1bΔC to respond to increased actomyosin tension within the YSL is unlikely to be due to ZO-1bΔC being degraded or non-functional, as the total expression level of these two ZO-1 versions were comparable (Figure S6A-A').

To further determine whether ZO-1b directly binding to actin is needed for TJ mechanosensitivity, we substituted full-length ZO-1b with ZO-1bΔABR, lacking its actin binding region within the C-terminus, by expressing ZO-1bΔABR in MZ*zo-1b/3* mutant embryos. Interestingly, we found that non-junctional ZO-1bΔABR clusters displayed retrograde flow within the YSL similar to clusters

formed by full-length ZO-1b (Figure S5D-D''), suggesting that direct binding of ZO-1b to actin is not required for it to undergo actomyosin-contraction dependent retrograde flow within the YSL. However, accumulation of non-junctional ZO-1bΔABR clusters close to the EVL-YSL boundary (Figure S5E-E') and stable incorporation of ZO-1bΔABR clusters into TJ at this boundary were severely reduced with retrogradely flowing ZO-1bΔABR clusters - instead of being incorporated into TJ once arriving at the EVL-YSL boundary (Figure S6B-B', Video S6) - frequently 'bypassing' this boundary or detaching from the junctional pool (Figure S6C-C''). Analysis of the subcellular distribution of ZO-1bΔABR clusters within the YSL further revealed that these clusters were not confined to the surface of the YSL, where the actomyosin cortex is located and most of the full-length ZO-1b clusters were found (Figure S6C-C''), but more broadly distributed throughout the YSL (Figure S6C''). This led to some of the ZO-1bΔABR clusters flowing below the TJ complex at the EVL-YSL boundary thereby bypassing this boundary and not being stably incorporated into the TJ (Figure S6C-C''). To test whether this reduced junctional incorporation of ZO-1bΔABR interferes with TJ mechanosensitivity, we increased YSL actomyosin tension by expressing caRhoA and analyzed how this affects junctional accumulation of ZO-1bΔABR. Interestingly, we found that the increase in junctional levels of ZO-1bΔABR in response to increased actomyosin tension and flow within the YSL was much less pronounced than observed for full-length ZO-1b (Figure 6C-C'). This suggests that direct binding of ZO-1b to the actomyosin cortex confines non-junctional ZO-1b clusters to the YSL surface, where they can be most effectively incorporated into the TJ at the EVL-YSL interface.

Importantly, while substituting full-length ZO-1b with forms that can either not form phase-separated clusters (ZO-1bΔC) or cannot directly bind actin (ZO-1bΔABR) abolished the effect of increased actomyosin tension on junctional accumulation of ZO-1b, both forms of ZO-1b still showed a substantial base-level junctional accumulation at the EVL-YSL boundary. This suggests that the formation, retrograde flow and junctional incorporation of ZO-1b clusters are needed to tune the amount of junctional ZO-1b at EVL-YSL boundary with the tension of the associated YSL actomyosin cytoskeleton, but not for the general accumulation of junctional ZO-1b at this boundary.

TJ mechanosensitivity is required for EVL spreading

Finally, we tested whether TJ mechanosensitivity is required for normal EVL epiboly movements. To this end, we attempted to rescue the epiboly phenotype of *zo-1b/3* YSL morphant embryos by injecting mRNA for either the full-length and thus mechanosensitive ZO-1b or the mechano-insensitive ZO-1bΔC and ZO-1bΔABR versions. Strikingly, we found that while the full-length version of ZO-1b in combination with ZO-3 could partially rescue the delay in epiboly progression and actomyosin ring formation in the morphant (Figures 6D-D',E-E' and 2C-C'), expression of ZO-1bΔC or ZO-1bΔABR together with ZO-3 at the same stoichiometric ratios as their full-length counterpart failed to rescue these phenotypes (Figure 6D-D',E-E' and S6D-D'). This suggests that the C-terminus and, specifically, the ABR therein, is important for ZO-1b function in EVL-YSL epiboly movement, and - given that these parts of ZO-1b are also required for ZO-1b mechanosensitivity - that ZO-1b mechanosensitivity is important for EVL-YSL epiboly progression.

Discussion

Our study provides direct evidence that TJ mechanosensitivity is achieved by contractility-driven cortical actomyosin flow transporting phase-separated non-junctional ZO-1b clusters towards the junction. Recent biochemical evidence from *in vitro* reconstitution and cell culture experiments suggest that ZO proteins, like other members of the MAGUK family (Zeng et al. 2016), can undergo phase separation (Beutel et al., n.d.). Our data support these observations by showing that ZO-1b can undergo phase separation within the YSL. Importantly, the ability of ZO-1b to undergo phase separation seems to be required to form non-junctional clusters within the YSL, given that versions

of ZO-1b incapable of undergoing phase separation, such as ZO-1bΔC (Beutel et al., n.d.), failed to form those clusters. Whether other TJ proteins also undergo phase separation and/or localize to ZO-1b non-junctional clusters is not yet entirely clear. Our data so far suggest that TJ adhesion receptors, such as Occludins and Claudins, are exclusively localizing to TJ but do not form non-junctional clusters (Figures S6E-F and S1A-D). In contrast, the cytoskeletal adapter protein Cingulin-like 1/Paracingulin, previously shown to also localize to TJ (Citi, Pulimeno, and Paschoud 2012; Guillemot et al. 2014), colocalizes with both junctional and non-junctional ZO-1b (Figure S6G-G'). This points at the possibility that TJ adaptor proteins, but not adhesion receptors, can form non-junctional phase-separated clusters within the YSL. Our findings also suggest that ZO-1b can form phase-separated clusters even when it lacks its ABR, suggesting that actin binding is not a prerequisite for ZO-1b to undergo phase separation. However, actin binding seems to be important for ZO-1b clusters to take their characteristic elongated rod-like shapes, an effect most likely due to those clusters adhering and spreading on the filamentous actin network. Further, the presence of a functional actomyosin network appears to restrict the maximum size of ZO-1b clusters, consistent with previous studies showing that the mesh size of elastic polymers can tune the phase separation capacity (Style et al. 2018).

Besides influencing the shape of ZO-1b clusters, binding to actin also appears to be critical for ZO-1b mechanosensation, given that ZO proteins that lack their ABR within the C-terminus, such as ZO-1b**Δ**ABR, failed to respond to changes in actomyosin tension. This loss of mechanosensitivity is likely due to ZO-1b**Δ**ABR clusters being less effectively incorporated into TJ, an effect presumably caused by ZO-1b**Δ**ABR clusters being less confined to the surface of the YSL and thereby flowing below the TJ without being integrated. Additionally, ZO-1b**Δ**ABR showed reduced junctional stability with clusters frequently dissociating from the EVL-YSL junction. Interestingly, ZO-1 lacking its ABR has previously found to display reduced junctional immobilization (Yu et al. 2010), supporting the view that actin binding promotes the stable junctional incorporation of ZO-1. Furthermore, our observation that the retrograde flow of ZO-1b**Δ**ABR clusters within the YSL was largely unaffected suggests that ZO-1 binding to actin is predominantly required for localizing non-junctional ZO-1 clusters to the YSL surface and not transporting it towards the EVL-YSL boundary. How the retrograde flow of non-junctional ZO-1 clusters within the YSL is achieved is not yet entirely clear, but it is conceivable that advection of the YSL cytoplasm caused by the flow of the actomyosin network might be involved.

TJ mechanosensitivity is likely to be important for both junctional signaling and mechanics at the EVL-YSL boundary. Foremost, it might be required for triggering the formation and maturation of the contractile actomyosin band within the YSL by establishing a positive feedback loop, where actomyosin contractility and flow promotes TJ formation (Zihni et al. 2016), and TJ promote actomyosin contractility and flow. Our observation that TJ and actomyosin ring formation at the EVL-YSL boundary are interdependent processes, clearly supports this notion. Interestingly, we have only detected retrograde actomyosin and TJ protein flows towards the EVL-YSL junction on the side of the YSL, but not at the leading edge of EVL forming the other side of the contact. While this might be due to technical limitations in imaging such flows in EVL cells that are much smaller than the yolk cell, it is also conceivable that TJ mechanosensitivity is restricted to the side of the YSL. How such potential asymmetric mechanosensitive regulation of TJ at the EVL-YSL boundary affects the biochemical and mechanical function of this junction is not yet clear, but binding of adhesion receptors over the contact might trigger non-autonomous effects eventually equilibrating the amount of TJ components on both sides of the EVL-YSL boundary.

TJ mechanosensitivity might also be required for TJ mechanically linking the EVL margin to the YSL by balancing the coupling strength of TJ to the mechanical force applied to this junction by the

contractile actomyosin network within the YSL. Such function has been demonstrated for AJ where junctional tension leads to conformational changes of α-catenin and vinculin, which again increases the actin-binding capability of these AJ components to the adjacent actomyosin cortex (Gomez, McLachlan, and Yap 2011). While the role of TJ in regulating cell-cell coupling strength remains largely unknown, recent studies showing that the TJ component ZO-1 modulates tension at cell-cell junctions (Tornavaca et al. 2015; Hatte, Prigent, and Tassan 2018) and can be stretched by tension (Spadaro et al. 2017), suggest that ZO proteins are involved in force transduction and reception at cell-cell contacts (Hashimoto et al. 2019). Our observation that TJ appear to be the predominant junction type at the EVL-YSL boundary, and that there is force transduction from the actomyosin band within the YSL to the leading edge of the EVL (Behrndt et al. 2012) point at the possibility that TJ have a force-transducing function. Whether and how forces are being transmitted by TJ, and how mechanosensitive junction growth affect such potential function remains to be investigated.

Interestingly, previous studies have suggested that the C-terminus of ZO-1 can fold back on its N-terminal part in an auto-inhibitory fashion, and that this auto-inhibition can be released by ZO-1 binding to and being stretched by the contractile actomyosin network, thereby allowing it to bind to other junctional proteins (Spadaro et al. 2017). This might explain why versions of ZO-1b lacking either their ABR or entire C-terminus are unable to rescue the epiboly phenotype of *zo-1b/3* YSL morphant embryos: their failure to directly bind to the actin cytoskeleton might not only diminish their localization to the YSL surface and thus their effective incorporation into TJ at the EVL-YSL boundary, but might also interfere with tension-induced conformational changes of ZO-1b required for its biological activity. Future experiments aimed at a systematic structure-function analysis of different ZO proteins will be needed to determine which regions, in addition to the ABR within the C-terminus, binding directly or indirectly to the actin cytoskeleton, are needed to confer mechanosensitivity to those proteins. It will also be interesting to investigate how phase separation at the membrane is initiated - whether clusters form spontaneously through random fluctuations or through pre-existing structures leading to heterogeneous nucleation events (Hyman, Weber, and Jülicher 2014), or whether there is any additional fine-tuning of critical concentration levels or phase separation capacity via post-translational modifications (Alberti 2017; Monahan et al. 2017) of ZO proteins.

There is increasing evidence for mechanochemical feedback loops forming the basis of various developmental processes (Goehring and Grill 2013; Hannezo and Heisenberg 2019). A key feature of those feedback loops is the interdependency of mechanical and chemical signals, the concerted action of which drive key cellular processes, such as cell polarization and migration. While the biochemical basis of force-generation and transmission is increasingly well understood (Lecuit, Lenne, and Munro 2011), comparable little is yet known about how mechanical forces feed back on biochemical processes. Our findings of mechanical forces promoting the growth of TJ through the generation of actomyosin flow not only unravels that TJ, similar to AJ, are mechanosensitive, but also more broadly points at a yet unrecognized role of TJ in controlling tissue mechanics within the developing organism.

Acknowledgements

We thank Ashley Bruce for the Claudin-D construct, Alf Honigmann for sharing unpublished data and providing GFP protein, the Heisenberg group for fruitful discussions, the Bioimaging and Zebrafish Facilities of IST Austria for their continuous support, and Robert Hauschild, Christoph Sommer, and Lenka Matejovicova for their help with image analysis. We are also particularly grateful to the late Suzanne Eaton for discussions on the initial idea of phase separation in the context of tight junction formation. This project was supported by funding from the European Union (European Research

Council Advanced Grant 742573) to C.-P.H. and the Biotechnology and Biological Sciences Research Council (BBSRC - BB/N014855/1) to M.B., M.T. and K.M.

Author contributions

C.S. and C.-P.H. designed the research. C.S. performed the experiments and analyzed the experimental data; S.S., K.P.-F. and A.S. contributed to the experimental work and data analysis. M.B., M.T. and K.M. provided reagents and conceptual input. C.S., C.-P.H., M.B., M.T. and K.M. wrote the manuscript.

Declaration of Interests

The authors declare no competing interests.

Figure 1. Tight junction components accumulate at the EVL-YSL boundary

(A) Schematic representation of enveloping layer (EVL) spreading during consecutive stages of epiboly (4-5, 6 and 8 hpf). Yolk cell, light grey; blastoderm (EVL and deep cells), dark grey. Black rectangle demarcates region of enlarged sagittal view outlining the tissue structure at 8 hpf. Red rectangle demarcates regions of the EVL-YSL boundary shown in (B).

(B) Maximum intensity projections (MIPs) of F-actin (Phalloidin, 1st row), ZO-1 (2nd row), ZO-3 (3rd row), E-Cadherin (4th row), and β-Catenin (5th row) localization at the EVL-YSL boundary at 4-5 hpf (left column), 6 hpf (middle column) and 8 hpf (right column). ZO-1, ZO-3, E-Cadherin and β-Catenin were detected by immunohistochemistry. White arrowheads point to increased accumulation at the EVL-YSL boundary. Scale bar, 20 μm.

(C) Plot of EVL-YSL junctional intensity normalized to EVL-EVL junctional intensity as a function of time during EVL epiboly (see also schematic above). Data are mean at 95% confidence. F-actin with N=2 and n=15 cells at 4-5 hpf, n=42 cells at 6 hpf and n=46 cells at 8 hpf. ZO-1 with N=2 and n=15 cells at 4-5 hpf, n=42 cells at 6 hpf and n=46 cells at 8 hpf. ZO-3 with N=2 and n=26 cells at 4-5 hpf, n=52 cells at 6 hpf, n=58 cells at 8 hpf. E-Cadherin with N=3 and n=29 cells at 4-5 hpf, with N=2 and n=32 cells at 6hpf, N=3 and n=84 cells at 8 hpf. β-Catenin with N=2 and n=54 cells at 4-5 hpf, n=29 cells at 6 hpf, n=28 cells at 8 hpf.

(D) Plot of EVL-YSL junctional intensity (black) and EVL-EVL junctional intensity (grey) normalized to cytoplasmic intensity at 8hpf. Red dashed line indicates ratio of 1 demarcating the boundary between accumulation (>1) and depletion (<1). Data are mean at 95% confidence. F-Actin and ZO-1 with N=2 and n=46 cells, ZO-3 with N=2 and n=58 cells. E-Cadherin with N=2 and n=40 cells. β-Catenin with N=2 and n=28 cells. Statistical test for F-Actin, ZO-3 and E-Cadherin, Mann-Whitney test with ****$p < 0.0001$; ZO-1 and β-Catenin, Unpaired t test with ****$p < 0.0001$.

See also Figure S1.

Figure 2. ZO-1b and 3 are required for proper EVL epiboly movements, and actomyosin flows and tension within the YSL

(A,B) Maximum intensity projections (MIPs) of brightfield/fluorescence images of embryos injected directly into the YSL at high stage (3.3 hpf) with phenol red and *H2A*-mcherry mRNA (Ctrl, left panel), *zo-1b* MO (1.5 ng) and *zo-3* MO (0.5 ng) (middle panel), and *zo-1b/3* MO together with GFP-tagged *zo-1b* mRNA (25 pg) and GFP-tagged *zo-3* mRNA (mutated for MO recognition site, 5 pg) (right panel) at 9 hpf (A) and wild-type (wt) control embryos (Ctrl, left panel), MZ*zo-1b/3* mutant (middle panel) and morphant embryos (injected with 1.5 ng of *zo-1b* MO and 0.5 ng of *zo-3* MO at 1-cell stage, right panel) at 9 hpf (B). Plasma membrane is marked by membrane-RFP to outline cells. EVL-YSL boundary is marked by white dashed line to demarcate extent of EVL epiboly in the different conditions. Schemes of different injection methods showing injection into the YSL (A) to obtain YSL-specific knock-down and into the 1-cell stage embryo (B) to gain ubiquitous knock-down. Scale bar, 200 μm.

(A', B') Plot of total time required for EVL to complete epiboly for the conditions shown in (A,B) and normalized to average time needed by control embryos. (A') YSL-Ctrl in black with N=3, n=11 embryos; YSL-morphant in cyan with N=3, n=12 embryos; and YSL morphant rescue in magenta with N=3, n=11 embryos. (B') wt control in black with N=4, n=11 embryos and 1-cell stage injected controls in black for morphant with N=3, n=11 embryos; mutant in cyan with N=4, n=13 embryos, and morphant in magenta with N=3, n=8 embryos. Data are shown as box-and-whisker plots (Whiskers: Tukey). Ordinary one-way ANOVA with Tukey's multiple comparisons test with ****$p < 0.0001$, ***$p < 0.001$ (A') and one-way ANOVA with Tukey's multiple comparisons test ****$p < 0.0001$ (B').

(A'',B'') Plot of EVL tissue spreading, expressed as height of EVL (h_{EVL}) normalized to total embryo height (h_{TOT}), as a function of time normalized to average time needed by control embryos for the conditions shown in (A,B). N/n as in (A',B'). Data are mean ± s.e.m.

(C) MIPs of Myosin-2 localization at the EVL-YSL boundary in Tg(*actb1:myl12.1-eGFP*) or Tg(*actb1:myl12.1-mcherry*) YSL-Ctrl (phenol red injected), *zo-1b/3* YSL-morphant (1.5ng, 0.5 ng into

the YSL) and *zo-1b/3* YSL-morphant embryos rescued by co-injection of GFP-tagged *zo-1b* (25 pg) and *zo-3* (5 pg, mutated for MO recognition site) mRNAs at 7-8 hpf. Scale bar, 20µm.
(C') Plot of Myosin-2 intensity as a function of distance from EVL margin in YSL-Ctrl, *zo-1b/3* YSL-morphant and rescued *zo-1b/3* MO YSL-morphant embryos at 7-8 hpf. Fluorescence intensity was normalized to EVL cortical signal. Data are mean ± s.e.m. Unpaired t test with **p = 0.0012 and *p=0.0329. YSL-Ctrl with N=4, n=8 embryos and *zo-1b/3* YSL-morphant with N=5, n=8 embryos. Rescued *zo-1b/3* YSL-morphant with N=6, n=13 embryos.
(D) Kymograph of Myosin-2 flow velocities along the animal-vegetal (AV) axis of the embryo as a function of time during epiboly in an exemplary YSL-Ctrl, *zo-1b/3* YSL-morphant and *zo-1b/3* rescued YSL-morphant embryo at 7-8 hpf. Kymograph ranges from negative values (in blue and blue arrow) indicating retrograde flows towards the EVL margin to positive values (in red and red arrow) indicating anterograde flows towards the vegetal pole. Black dashed line indicates the slope of EVL movement of YSL-Ctrl embryos; EVL is located above dashed line and YSL below. Blue dashed line indicates EVL movement of *zo-1b/3* YSL-morphant embryo and pink dashed line indicates EVL movement of rescued *zo-1b/3* YSL-morphant embryo.
(D') Plot of Myosin-2 mean flow velocities along AV axis averaged over 7.5-30 min in YSL-Ctrl, *zo-1b/3* YSL-morphant and rescued *zo-1b/3* YSL-morphant embryos between 7 and 8 hpf. EVL peak velocities averaged over 10 µm, Unpaired t test, ****p < 0.0001; YSL peak velocities averaged over 45 µm (15 - 60 µm from EVL margin), Mann-Whitney test , ****p < 0.0001. N/n same as in (C'').
(E,F) MIPs of the EVL-YSL boundary in Myosin-2 expressing Tg(*actb1:myl12.1-eGFP*) YSL-Ctrl and *zo-1b/3* YSL-morphant (1.5 ng of *zo-1b* MO and 0.5ng of *zo-3* MO into the YSL) embryos at 7-8 hpf (E) and Tg(*actb1:myl12.1-eGFP*) expressing wt embryos at 6 and 8 hpf (F), after (4th post-cut frame) UV laser-cutting along a 5 µm line oriented perpendicular to the boundary. Scale bar, 10 µm.
(E',F') Exemplary kymographs of EVL-YSL junctional opening in response to UV-laser cutting as a function of time for the conditions shown in (E,F). Horizontal scale bar, 1.2 s; vertical scale bar, 1 µm.
(E'',F") Plot of initial recoil velocities of EVL-YSL junction after UV-laser cutting for the conditions shown in (E,F). Data are shown as box-and-whisker plots (whiskers: Tukey). Unpaired t test with ****p < 0.0001; **p = 0.0073. YSL-Ctrl and *zo-1b/3* YSL-morphant with each N=2, n=12 embryos. wt embryos at 6 hpf and 8 hpf with each N=3, n=17 embryos.
See also Figure S2 and Videos S1 and S2.

Figure 3. Actomyosin contractility affects ZO-1 recruitment to the EVL-YSL boundary
(A,B) Maximum intensity projections (MIPs) of F-actin (Phalloidin, 1st row) and ZO-1 (2nd row) localization at the EVL-YSL junction in embryos that were either injected into the YSL at high stage (3.3 hpf) with *H2A-mcherry* mRNA (100pg, left column, Ctrl) and *caMypt* mRNA (75pg *caMypt* plus 25pg *H2A*-mcherry mRNA, right column) shown at 8 hpf (A), or injected into marginal blastomeres/YSL at 128-cell stage with *H2B*-EGFP mRNA (2.3-2.5 pg - left column, Ctrl) and *caRhoA* mRNA (0.3-0.5 pg *caRhoA* plus 2 pg *H2B-GFP*, right column) shown at 6 hpf (B). ZO-1 was detected by immunohistochemistry. White arrowheads point to decrease (A) or increase (B) in signal at the EVL-YSL boundary. Scale bar, 20 µm.
(A',B') Plot of junctional ZO-1 intensity ratio (EVL-YSL/EVL-EVL) for the conditions described in (A,B). (A) Ctrl with N=2, n=44 cells; *caMypt* mRNA YSL-injected embryos with N=2, n=39 cells. (B) Ctrl YSL-injected embryos with N=2, n=28 cells; *caRhoA* mRNA YSL-injected with N=2, n=52 cells. Data are shown as mean plus s.e.m.; Mann-Whitney test; ** p = 0.006 (A'), ***p = 0.0007 (B').
(A",B") Plot of non-junctional ZO-1 fluorescent intensity as a function of distance from the EVL margin for the conditions shown in (A,B). Data are shown as mean plus s.e.m. Unpaired t test of non-junctional pool within first 5 µm from EVL margin with ****p < 0.0001 (A). Mann-Whitney test of non-junctional ZO-1 within first 5 µm from EVL margin with ****p < 0.0001 (B). (A'') Ctrl with N=2, n=6 embryos; caMypt with N=2,n=7 embryos. (B'') Ctrl with N=2, n=6 embryos; caRhoA with N=2, n=9 embryos.
See also Figure S3.

Figure 4. Non-junctional clusters of ZO-1b within the YSL undergo retrograde flows and are incorporated into TJ at the EVL-YSL boundary

(A,B) Maximum intensity projections (MIPs) of Myosin-2 (A) or ZO-1b (B) localization at the EVL-YSL boundary in Tg(*actb1:myl12.1-mcherry*; *actb1:mNEONgreen-zo-1b*) embryos at 7-8 hpf. Scale bar, 20 µm.

(A',B') Exemplary kymographs of Myosin-2 (A') or ZO-1b (B') flow velocities along the animal-vegetal (AV) axis of the YSL as a function of time during epiboly. Kymograph ranges from negative (retrograde flows towards the EVL-YSL boundary, blue) to positive (anterograde flows away from the EVL-YSL boundary, red) values.

(A'',B'') Maximum Myosin-2 (A") and ZO-1b (B") flow velocities, indicating peak retrograde flow rates within the YSL (negative value) and maximum epiboly movement velocity of the EVL-YSL boundary (positive value). N=4, n=7 embryos. Mann-Whitney test, ns not significant.

(C) Consecutive MIP high-resolution (Airy Scan) images of non-junctional ZO-1b being incorporated at the EVL-YSL boundary (indicated by white arrow head) in a Tg(*actb1:mNEONgreen-zo-1b*) embryo at 7-8 hpf. Horizontal scale bar, 48 sec; Vertical scale bar, 2 µm. Calibration bar showing LUT for grey value range.

(C') Kymograph of boxed region in (C) showing non-junctional ZO-1b cluster (black arrowhead) incorporation at the EVL-YSL boundary (pink arrowhead). Horizontal scale bar, 40 sec; vertical scale bar, 1 µm.

(D) Consecutive MIP high-resolution (Airy Scan) images of non-junctional ZO-1b clusters undergoing fusion close to the EVL-YSL boundary (within 15 µm distance to EVL) in a Tg(*actb1:mNEONgreen-zo-1b*) embryo at 6.5-8 hpf. White dashed circle shows region of fusing non-junctional clusters. Scale bar, 500 nm. Calibration bar showing LUT for grey value range.

(D') Plot of average ZO-1b non-junctional cluster size normalized to initial average size within the YSL as a function of time between 5.7-8 hpf. Cluster size was averaged over acquisition times of 20 sec +/- 5.5 s. N=5, n=9 embryos.

(D'') Plot of cumulative fusion events per ZO-1b cluster as a function of time in Tg(*actb1:mNEONgreen-zo-1b*) embryos at 6-8 hpf. Each line represents fusion events averaged per embryo. N=5, n=15 embryos.

(E,F) Sum intensity projection image (sum of all slices) of ZO-1b signal in Tg(*actb1:mNEONgreen-zo-1b*) embryos within the YSL (2-5 µm from EVL margin) (E with N=4, n=13 embryos and F with N=4, n=12 embryos) after bleaching in FRAP experiments at early-mid (5-6 hpf; E) and late epiboly stage (7-8 hpf; F). White dashed box outlines bleached region. Scale bar, 5 µm.

(E',F') Exemplary kymograph of bleached region for the conditions described in (E,F). White dashed box outlines region used for intensity measurements. Horizontal scale bar, 40 s; vertical scale bar, 1 µm.

(E",F") Plot of GFP-ZO-1b fluorescence recovery as a function of time for the conditions described in (E,F). Data are mean ± SD. Intensity values were normalized to the pre-bleach intensities and to non-junctional signals (E,F) to correct for bleaching (more details see Materials and Methods). Solid line shows a double exponential fit (E'',F'').

See also Figure S4 and Videos S3 and S4.

Figure 5. Non-junctional ZO-1b undergoes phase separation within the YSL

(A) MIP high-resolution (Airy Scan) images of non-junctional GFP-ZO-1b clusters within the YSL of MZ*zo-1b/3* mutants injected at 1-cell with different concentrations of *GFP-zo-1b* mRNAs (50 pg - 150 pg mRNA) at 7-8 hpf. 1st row, GFP signal only; 2nd row, GFP signal (green) overlaid with white signal obtained by cluster masking using Ilastik (for details see Materials and Methods). ZO-1b concentrations in µM were determined via quantitative fluorescence microscopy. Calibration curves (see Figure S5A) were acquired with the same imaging settings. Intensity for image of 1 µM ZO-1b concentration was enhanced for displaying the small and less intense clusters better. Scale bar, 2 µm.

(A') Plot of average area of ZO-1b clusters as a function of ZO-1b concentration. N=3, n=33 embryos.

(A'') Bar plot of average fusion rate per ZO-1b cluster for different ZO-1b concentrations within the YSL. Average fusion rate was determined as the total fusion number divided by the average cluster number in a time window of 3 min. Data are shown as box-and-whisker plots (Whiskers: Tukey). Mann Whitney test. ***p = 0.001. N=3, n=32 embryos.
(A''') Plot of cumulative fusion events per ZO-1b cluster as a function of time. Curves show the different ZO-1b concentrations. Data are shown as mean plus s.e.m. N/n see (A'').
(B) Schematic representation of the domain structure of full length ZO-1b, ZO-1b**Δ**C construct, lacking its mainly intrinsically disordered C-terminus including an Actin binding region (ABR) and ZO-1b**Δ**ABR construct, only lacking the ABR within the IDR.
(C) MIP high-resolution (Airy Scan) images of MZ*zo-1b/3* mutant embryos injected at 1-cell stage with either *GFP-zo-1b* (50 pg, Ctrl) or *GFP-zo-1b**Δ**C* (30 pg) mRNAs at 8 hpf. Scale bar, 2 µm.
(D,E) MIP high-resolution (Airy Scan) images of non-junctional ZO-1b clusters within the YSL of MZ*zo-1b/3* mutants injected at 1-cell stage with either *GFP-zo-1b* (50 pg, control) or *GFP-zo-1b**Δ**ABR* (44 pg) at 7-8 hpf (D). MIP high-resolution (Airy Scan) images of Tg(*actb1:mNEONgreen-zo-1b*) embryos treated for 1h with either DMSO (Ctrl) or 1 µg/ml Latrunculin B prior to imaging at 5.3-6.3 hpf (E). 1st row, GFP signal only; 2nd row, GFP signal (green in D or white in E) overlaid with white (D) or red (E) signal obtained by cluster masking using Ilastik (for details see Materials and Methods). Scale bar, 2 µm.
(D') Bar plot of average fusion rate per ZO-1b and ZO-1b**Δ**ABR cluster within the YSL. Average fusion rate was determined as the total fusion number divided by the average cluster number in a time window of 3 min. Data are shown as box-and-whisker plots (Whiskers: Tukey); Mann Whitney test; ns. not significant. ZO-1b with N=4, n= 8 embryos. ZO-1b**Δ**ABR with N=4, n=12 embryos.
(D'') Plot of cumulative fusion events per cluster as a function of time for ZO-1b and ZO-1b**Δ**ABR. Data are shown as mean plus s.e.m. N/n see (D').
(D''',E') Bar plot of average ZO-1b cluster area for the conditions described in (D and E). Data are shown as box-and-whisker plots (Whiskers: Tukey). Average Area of (D''') with unpaired t test, ns, not significant, p=0.0924. GFP-ZO-1b with N=6, n=9 embryos; GFP-ZO-1b**Δ**ABR with N=5, n=14 embryos. Average area of (E') with unpaired t test, *p = 0.0121. DMSO Ctrl with N=4, n=8 embryos; LatB with N=4, n=9 embryos.
(D'''',E'') Bar plot of average ZO-1b cluster circularity for the conditions described in (D and E). Circularity of clusters above 0.15 µm^2 area were analyzed. Data are shown as box-and-whisker plots (Whiskers: Tukey). A circularity value of 1 reflects a perfect circle, while values close to 0 indicate more elongated shapes. Circularity of (D'''') with unpaired t test *p = 0.0332. GFP-ZO-1b with N=6, n=9 embryos; GFP-ZO-1b**Δ**ABR with N=5, n=12 embryos. Circularity of (E'') with Mann-Whitney test, ***p=0.0004. DMSO Ctrl with N=4, n=6 embryos; LatB with N=4, n=9 embryos.
(F) Consecutive MIP high-resolution (Airy Scan) images of ZO-1b clusters undergoing fusion within the YSL of Tg(*actb1:mNEONgreen-zo-1b*) embryos treated for 1h with 1 µg/ml Latrunculin B prior to imaging at 5.3-6.3 hpf. Scale bar, 1 µm.
See also Figure S5 and Video S5.

Figure 6. Mechanosensitive response of ZO-1b is dependent on its C-terminus
(A,B,C) Maximum intensity projections (MIPs) of GFP-tagged ZO-1b (50 pg) (A), GFP-tagged ZO-1b**Δ**C (30 pg) (B) and GFP-tagged ZO-1b-**Δ**ABR (44 pg) (C) localization at the EVL-YSL boundary in MZ*zo-1b/3* embryos injected with *H2A*-mCherry mRNA (Ctrl - 2.3-2.5 pg *H2A*-mCherry; A with N=5, n=23 cells; B with N=4, n=43 cells; C with N=3, n=17 cells; two columns on the left) and embryos injected with *caRhoA* mRNA (0.3-0.5 pg caRhoA plus 2 pg H2B-GFP) specifically within the YSL (A with N=3, n=19 cells; B with N=3, n=13 cells; C with N=3, n=27 cells; two columns on the right) at the onset of imaging (7 hpf) (0 min; 1st and 3rd column) and 24 min later (2nd and 4th column). White arrowhead points to increased accumulation at the EVL-YSL boundary. Scale bar, 10 µm.
(A',B',C') Plot of EVL-YSL junctional intensity normalized to EVL-EVL junctional intensity as a function of time during EVL epiboly in the conditions described in (A,B,C). Data are mean ± s.e.m.

(D,E) MIPs of brightfield/fluorescence images of embryos injected directly into the YSL at high stage (3.3 hpf) with phenol red and *H2A-mcherry* mRNA (Ctrl in D with N=8, n=27 embryos, Ctrl in E with N=3, n=10 embryos), *zo-1b/3* MO (1.5 ng *zo-1b* MO, 0.5ng *zo-3* MO, D with N=8, n=28 embryos; E with N=3, n=12 embryos) alone, *zo-1b/3* MO together with *GFP-zo-3* (5 pg) and GFP-*zo-1b* (25 pg) mRNA (D with N=8, n=27 embryos; E with N=3, n=8 embryos), and *zo-1b/3* MO together with *GFP-zo-3* (5 pg) and GFP-*zo-1b***Δ**C (15 pg) mRNA (D with N=8, n=26 embryos) or *zo-1b/3* MO together with *GFP-zo-3* (5 pg) and GFP-*zo-1b***Δ**ABR (22 pg) mRNA (E with N=3, n=8 embryos) at 9 hpf. Plasma membrane is marked by membrane-RFP to outline cells. EVL-YSL boundary is marked by white dashed line to demarcate extent of EVL epiboly in the different conditions. Scale bar, 100 μm.
(D',E') Plot of total time required for EVL to complete epiboly for the conditions shown in (D,E) and normalized to average time needed by control embryos. Data are shown as box-and-whisker plots (Whiskers: Tukey). One-way ANOVA with ****p < 0.0001; **p=0.0027; ns, non significant. For full-length rescue (Figure 6D-D') , data shown in Figure 2B' were included.
See also Figure S5, S6 and Video S6.

Figure S1. Tight junction and adherens junction component accumulation at the EVL-YSL boundary. Related to Figure 1.

(A) Schematic representation of EVL spreading during consecutive stages of epiboly (4-5, 6 and 8 hpf). Yolk cell, light grey; blastoderm (EVL and deep cells), dark grey. Red rectangle demarcates regions of the EVL-YSL boundary shown in (B).

(B) Maximum intensity projections (MIPs) of GFP-Cingulin-like 1 (1st row), GFP-Claudin-D (2nd row), GFP-Occludin-A (3rd row) and α-Catenin (4th row) localization at the EVL-YSL boundary at 4-5 (left column), 6 (middle column) and 8 (right column) hpf. α-Catenin is visualized by immunohistochemistry, Cingulin-like 1 and Claudin-D and Occludin-A by expression of their respective GFP- or mNEONgreen-fusion constructs, respectively, in wild type embryos injected with 15 - 50 pg mRNA at 1-cell stage. White arrowheads point to increased accumulation at the EVL-YSL boundary. Scale bar, 20 µm.

(C) Plot of EVL-YSL junctional intensity normalized to EVL-EVL junctional intensity as a function of time during EVL epiboly (see also schematic above). Data are mean at 95% confidence. Cingulin-like 1 with N=2 and n=33 cells at 4-5 hpf, n=37 cells at 6 hpf and n=31 cells at 8 hpf. Claudin-D with N=2, n=40 cells at 4-5 hpf, n=50 cells at 6 hpf, n=29 cells at 8 hpf. Occludin-A with N=2, n=27 cells at 4-5 hpf; N=2, n=54 cells at 6 hpf; N=3, n=43 cells at 8 hpf. α-Catenin with N=2 and n=45 cells at 4-5 hpf, n=29 cells at 6 hpf, n=28 cells at 8 hpf.

(D) Plot of EVL-YSL junctional intensity (black) and EVL-EVL junctional intensity (grey) normalized to cytoplasmic intensity at 8 hpf. Red dashed line indicates ratio of 1 demarcating the boundary between accumulation (>1) and depletion (<1). Data are mean at 95 % confidence. Cingulin-like 1 with N=2 and n=30. Claudin-D with N=2 and n=29 cells. Occludin-A with N=3, n=43 cells. α-Catenin with N=2 and n=28 cells. Cingulin, Claudin-D and Occludin-A with Mann-Whitney test with **p = 0.0073, ns, not significant; α-Catenin, Unpaired t test with ****p < 0.0001.

Figure S2. *zo-1b/3* mutant and morphant analysis. Related to Figure 2.

(A) Plot of total time required for EVL to complete epiboly normalized to the average time needed by control embryos injected with either phenol-red (Ctrl), *zo-1b/3* 5-base mismatch control MO (*zo-1b/3* MO) or standard negative control MO (standard control MO) into the YSL. Data are mean ± s.e.m. Kruskal-Wallis test with Dunn's multiple comparisons test. ns, not significant. Ctrl with N=4, n=14 embryos; *zo-1b/3* MO with N=3, n=12 embryos; standard control MO with N=3, n=11 embryos.

(B) Dorsal view of YSL-injected control (phenol-red, YSL-Ctrl) and *zo-1b/3* morphant (YSL-morphant) embryos at 1-somite stage (10.5 hpf) labeled by in situ hybridization for *papc* outlining the forming somites. Scale bar, 200 µm.

(B') Bar plot of stage distribution (categorized in 0 and 1 somite stages as revealed by *papc* in situ hybridization) for the conditions described in (B). Data are mean ± s.e.m. 80% of Ctrl-YSL embryos and 69% of *zo-1b/3* YSL-morphants showed 1 somite at 10.5 hpf. Mann-Whitney test with n.s.; not significant. YSL-Ctrl with N=3, n=36 embryos; YSL-morphant with N=3, n=45 embryos;

(C) Mutation sites in MZ*zo-1b* and MZ*zo-3* mutants. Red triangles indicate the insertion sites of the STOP codon.

(D) Plot of EVL tissue spreading, expressed as height of EVL (h_{EVL}) normalized to total embryo height (h_{TOT}), as a function of time normalized to average time needed by control embryos shown for wild-type (wt) control, and MZ*zo-1b* and MZ*zo-3* single mutants. Data are mean ± s.e.m. One-way ANOVA with Tukey's multiple comparisons test. ns. not significant. Wt (Ctrl) with N=4, n=27 embryos; MZ*zo-1b* with N=3, n=16 embryos; and MZ*zo-3* with N=3, n=18 embryos.

(E) Dorsal view of control (phenol-red, Ctrl) and *zo-1b/3* morphant embryos (morphant) injected at the one-cell stage, and of wild-type (wt) and MZ*zo-1b/3* mutant embryos labeled at 10.5 hpf by in situ hybridization for *papc* outlining the forming somites. Scale bar, 200 µm.

(E') Bar plot of stage distribution (categorized in 0, 1 and 2-somite stages as revealed by *papc* in situ hybridization) for the condition described in (E). 86% of Ctrl, 67% of MZ*zo-1b/3* embryos and 73% of *zo-1b/3* morphants showed 1 somite at 10.5 hpf. Data are mean ± s.e.m. Cumulative link mixed model (Christensen 2018) was used to determine p-values in R. Ctrl vs. MZ*zo-1b/3* mutants with p =

0.0002 and Ctrl vs. *zo-1b/3* morphants with p = 0.04. Ctrl with N=2, n=26 embryos; morphant with N=3, n=43 embryos; wt Ctrl with N=4, n=72 embryos and mutant with N=5, n=77 embryos.
(F) Maximum intensity projections (MIPs) of ZO-1 (left column), ZO-3 (middle column) and E-cadherin (right column) localization at the EVL-YSL boundary in YSL-Ctrl (upper row) and *zo-1b/3* YSL-morphant (lower row) embryos at 8 hpf. ZO-1, ZO-3 and E-Cadherin were detected by immunohistochemistry. Scale bar, 20µm.
(F') Plot of EVL-YSL junctional intensity normalized to EVL-EVL junctional intensity at 8 hpf for the conditions described in (F). Data are mean ± s.e.m. Statistical test for ZO-1 intensity with Mann-Whitney test, ****p < 0.0001; ZO-3 intensity with unpaired t test, ****p < 0.0001; and E-Cadherin intensity with unpaired t test with **p = 0.0029; ZO-1: N=2, YSL-Ctrl with n=30 cells and *zo-1b/3* YSL-morphant with n=40 cells; ZO-3: N=2, YSL-Ctrl with n=42 cells and *zo-1b/3* YSL-morphant with n=59 cells. E-Cadherin: N=3, Ctrl with n=51 cells and *zo-1b/3* YSL-morphant with n=54 cells.
(G) MIPs of ZO-1 (left column), ZO-3 (middle column) and F-actin (right column) localization at the EVL-YSL boundary in wt (upper row - Ctrl) and MZ*zo-1b/3* mutant (lower row) embryos at 8 hpf. ZO-1 and ZO-3 were detected by immunohistochemistry, and F-actin by Phalloidin. ZO-1 antibody likely detects both zebrafish ZO-1a and ZO-1b, suggesting that the remaining signal in the MZ*zo-1b/3* mutant reflects ZO-1a protein expression.
(G') Plot of EVL-YSL junctional intensity normalized to EVL-EVL junctional intensity, and EVL-YSL junctional intensity together with EVL-EVL junctional intensity normalized to cytoplasmic intensity at 8 hpf for the conditions shown in (G). Data are mean ± s.e.m. Statistical test for ZO-1: EVL-YSL/EVL-EVL with Mann-Whitney test ****p < 0.0001, and EVL-YSL/cyto and EVL-EVL/cyto with unpaired t-test with ****p < 0.0001; ZO-3: EVL-YSL/cyto and EVL-EVL/cyto with unpaired t-test with ****p < 0.0001. N=2, wt with n=31 cells and MZ*zo-1b/3* mutant with n=33 cells.
(G'') Plot of F-Actin fluorescence intensity within the YSL as a function of distance from EVL margin for the conditions described in (D). F-actin was detected by Phalloidin. [a.u.], arbitrary units. N=2, wt with n=7 embryos and MZ*zo-1b/3* mutant with n=7 embryos.
(H) Compensatory expression changes of *zo* genes in MZ*zo-1b/3* mutant embryos normalized to the expression level of a housekeeping gene (*elongation factor 1α*). Fold change reflects the relative change of expression levels in MZ*zo-1b/3* mutant compared to wt embryos in qRT-PCR. Red solid line indicates 1-fold change in expression, demarcating the boundary between increase (>1) and decrease (<1) of expression levels of the five different *zo* genes (N=3).
(I,J) Plot of junctional opening (distance in µm) of the EVL-YSL boundary marked by Myosin-2-GFP after UV laser cutting at late (8 hpf) stage of EVL epiboly in YSL-Ctrl and *zo-1b/3* YSL-morphant (I) embryos and in wt embryos (J) at mid (6 hpf) and late (8 hpf) stages of EVL epiboly as a function of time after cutting. Red dashed boxes indicate regions for calculation of initial recoil velocity shown in (I',J').
(I',J') Plot of the first four time-points from (I,J) with linear fit to extract initial recoil velocity shown in (Figure 2E'', 2F''). N,n see (Figure 2E-F).

Figure S3. Effects of actomyosin contractility on its flow rate and AJ protein recruitment to EVL-YSL boundary. Related to Figure 3.
(A,C) MIPs of Myosin-2 localization at the EVL-YSL boundary in Tg(*actb1:myl12.1-eGFP*) embryos that were either injected into the YSL at high stage (3.3 hpf) with *caMypt* mRNA (75pg *caMypt* plus 25pg *H2A-mcherry* mRNA, right column) shown at 8 hpf (A), or injected into marginal blastomeres/YSL at 128-cell stage with *H2A*-mcherry mRNA (2.3-2.5 pg) and *caRhoA* mRNA (0.3-0.5 pg *caRhoA* mRNA plus 2 pg *H2A-mcherry* mRNA) shown at 6-7 hpf (C). Scale bar, 20 µm.
(A',C') Plot of Myosin-2 intensity as a function of distance from EVL margin in *caMypt* (A'), Ctrl and *caRhoA* (C') mRNA YSL-injected embryos at 7-8 hpf and 6-7 hpf, respectively. Fluorescence intensity was normalized to EVL cortical signal. Data are mean ± s.e.m. Mann-Whitney test with **p = 0.0031 (A'); *p = 0.0303 (C'). For N/n of YSL-Ctrl see (Figure 2C'). *caMypt* mRNA YSL-injected embryos with N=3, n=5 (A'); Ctrl with N=2, n=6 and *caRhoA* mRNA YSL-injected embryos with N=3, n=5 (C').

(B,D) Kymograph of Myosin-2 flow velocities along the animal-vegetal (AV) axis of the embryo as a function of time during epiboly in an exemplary *caMypt* mRNA YSL-injected embryo at 7-8 hpf (B), Ctrl and *caRhoA* mRNA YSL-injected embryo 6-7 hpf (D). Kymograph ranges from negative values (in blue), indicating retrograde flows towards the EVL margin, to positive values (in red), indicating anterograde flows towards the vegetal pole.
(B',D') Plot of Myosin-2 mean flow velocities along AV axis averaged over 10-30 min in *caMypt* mRNA YSL-injected embryos (B'), Ctrl (phenol-red) and *caRhoA* mRNA (D') YSL-injected embryos between 7-8 hpf and 6-7 hpf, respectively. YSL peak velocities were determined 15-60 µm from EVL margin. Statistical test for *caMypt*, Mann-Whitney test, ****p < 0.0001. Statistical test for *caRhoA*, Unpaired t test, ****p < 0.0001. N/n same as in (A',C').
(E) Maximum intensity projections (MIPs) of E-Cadherin (1st row) and β-Catenin (2nd row) localization at the EVL-YSL boundary in uninjected control embryos (Ctrl; first column) and embryos injected into the YSL with *caRhoA* (0.3-0.5 pg *caRhoA* plus 2pg *H2B*-EGFP) mRNA at 6 hpf (second column). E-Cadherin and β-Catenin were detected by immunohistochemistry. Scale bar, 20µm.
(E') Plots of E-cadherin and β-Catenin intensities at the EVL-YSL boundary normalized to EVL-EVL junctional intensity for the conditions described in (E). Mann-Whitney test, ns, not significant; E-cadherin and β-Catenin with N=2, control with n=31 cells and *caRhoA* mRNA YSL-injected embryos with n=27 cells.

Figure S4. Junctional ZO-1b dynamics. Related to Figure 4.
(A,B) Sum intensity projection image (sum of all slices) of GFP-ZO-1b signal in Tg(*actb1:mNEONgreen-zo-1b*) embryos at the EVL-YSL boundary (A with N=3, n=9 cells and B with N=2, n=10 cells) after bleaching in FRAP experiments at early-mid (5-6 hpf; A) and late epiboly stage (7-8 hpf; B). White dashed box outlines bleached region. Scale bar, 5 µm.
(A',B') Exemplary kymograph of bleached region for the conditions described in (A,B). White dashed box outlines region used for intensity measurements. Horizontal scale bar, 40 s; vertical scale bar, 1 µm.
(A",B") Plot of GFP-ZO-1b fluorescence recovery as a function of time for the conditions described in (A,B). Data are mean ± SD. Intensity values were normalized to the pre-bleach intensities and to reference junctional signals to correct for bleaching (more details see Materials and Methods). Solid line shows a double exponential fit (A'') and single exponential fit (B''). Double exponential fit was used at early-mid stage (6 hpf) due to the presence of two species (fast and slow species) of ZO-1b. Single exponential fit was used at late (8 hpf) stage, because only ~1% of fast species was detectable.

Figure S5. Interaction between ZO-1b and the actomyosin network within the YSL. Related to Figure 5.
(A) Calibration curve of fluorescence intensity normalized to laser power as a function of GFP protein concentration. a.u., arbitrary units. 0 µM (PBS) with N=3; 1 µM with N=1; 1.25 µM with N=2; 2.5 µM with N=2; 5 µM with N=2; 10 µM with N=3.
(B) Single plane fluorescence images of ZO-1b, Myosin-2 and an overlay of ZO-1b and Myosin-2 to visualize ZO-1b/Myosin-2 protein co-localization within the YSL of Tg(*actb1:myl12.1-mcherry*; *actb1:mNEONgreen-zo-1b*) embryo at 6-8 hpf. White boxes demarcate zoom-in region of examples of either mutual exclusive localization or co-localization of ZO-1b and Myosin-2. Scale bar, 2 µm (left panel) and 0.5 µm (right panel).
(B') Scatterplot of ZO-1b and Myosin-2 showing a wide signal spread indicative of partial colocalization (for more details see Material and Methods). Bar plot of Li's Intensity Correlation Quotient (ICQ) for colocalization quantification of ZO-1b and Myosin-2 between 6-8 hpf. Li's ICQ value ranges from 0.5 showing colocalization to -0.5 showing exclusion and values close to 0 indicate random localization. N=4, n=17 embryos.

(C) Maximum intensity projections (MIPs) of ZO-1b, Myosin-2 and Actin signals within the YSL of Tg(*actb1:myl12.1-mcherry*; *actb2:mNEONgreen-zo-1b*) *and Tg(actb2:NeonGreen-zo-1b) (actb2:Utrophin-mcherry)* embryos exposed for 1h to DMSO (control) and 1 µg/ml Latrunculin B followed by imaging from 5.3 to 6.3hpf. White dashed line shows exemplary line for plot in (C'). Scale bar, 2 µm.

(C') Line plots of Myosin-2 and Actin network intensity distribution within the YSL of 3 exemplary embryos each treated with DMSO or Latrunculin B (LatB). Note the strong decrease in signal between different Myosin-2 or Actin clusters upon LatB treatment (indicated with red arrow heads).

(D) MIPs of ZO-1b and ZO-1b-**Δ**ABR at the EVL-YSL boundary in *Tg(actb2:mNeonGreen-zo-1b) and Tg(actb2:mNeonGreen-zo-1b***Δ**ABR)* transgenic MZ*zo-1b/3* mutant embryos at 7-8 hpf. Scale bar, 20 µm.

(D') Kymograph of flow velocities of ZO-1b and ZO-1b-**Δ**ABR along the animal-vegetal (AV) axis of the embryo as a function of time during epiboly in exemplary embryos at 7-8 hpf. Kymograph ranges from negative values (in blue), indicating retrograde flows towards the EVL margin, to positive values (in red), indicating anterograde flows towards the vegetal pole.

(D'') Plot of mean flow velocities along AV axis averaged over 10-30 min for the conditions described in (D) between 7 and 8 hpf. ZO-1b with N=3, n=4 embryos, ZO-1b-**Δ**ABR with N=3, n=8 embryos.

(E,E') Plot of non-junctional fluorescence intensity of full-length ZO-1b (E) and ZO-1b-**Δ**ABR (E') as a function of distance from the EVL margin in MZ*zo-1b/3* mutant embryos injected with GFP-*zo-1b* (50 pg) and GFP-*zo-1b*-**Δ***ABR* (44 pg) mRNA in Ctrl conditions or after injection of 0.3-0.5 pg *caRhoA* mRNA into the YSL. Data are mean ± s.e.m. Mann-Whitney test for ZO-1b with *p=0.0175, not significant for ZO-1b-**Δ**ABR. Full-length ZO-1b: Ctrl with N=6, n=7 embryos and *caRhoA* mRNA YSL-injected with N=4, n=7 embryos. ZO-1b-**Δ**ABR: Ctrl with N=3, n=5 embryos and *caRhoA* mRNA YSL-injected with N=4, n=7 embryos.

Figure S6. Characterization of mechano-insensitive ZO-1b constructs and localization of TJ proteins. Related to Figure 6.

(A) Sum intensity projections (SUM) of GFP-ZO-1b and GFP-ZO-1bΔC localization in MZ*zo-1b/3* mutant embryos at the EVL-YSL boundary at 8 hpf. Scale bar 20 µm.

(A') Total intensity measurement normalized to laser power for the conditions described in (A). Data are shown as box-and-whisker plots (Whiskers: Tukey). Mann Whitney test; ns, not significant. ZO-1b with N=2, n=20 embryos; ZO-1bΔC with N=2, n=21 embryos.

(B) Sketch of how junctional integration efficiency (J_{ie}) was calculated: number of clusters merging and integrating with the EVL-YSL junction (J_i) subtracted by the number of clusters dissociating from the junction (J_d) and leaving towards the internal or external YSL.

(B') Bar plot of junctional ZO-1b cluster integration efficiency in MZ*zo-1b/3* mutant embryos injected with either GFP-*zo-1b* (50 pg) mRNA or GFP-*zo-1b***Δ***ABR mRNA (*44 pg) normalized to a 3 min time window.

(C) Snapshots of 3D tracking of ZO-1b and ZO-1b**Δ**ABR non-junctional clusters in MZ*zo-1b/3* mutant embryos injected with either GFP-*zo-1b* (50 pg) mRNA or GFP-*zo-1b***Δ***ABR mRNA (*44 pg) at the first and last time points at 7-8 hpf. The EVL movement was corrected in order to keep the EVL-YSL junction fixed in y at position 0 (see Materials and Methods). Scale bar, 2 µm.

(C') Single plane of yz of ZO-1b and ZO-1b**Δ**ABR cluster tracking with clusters typically being incorporated into the TJ for ZO-1b, and flowing below the TJ into the internal YSL or detaching from the junctional pool for ZO-1b**Δ**ABR (indicated by white arrow heads). White dashed line indicates apical side of YSL facing the outside. Scale bar, 1 µm (1st and 3rd row) and 2 µm (2nd row).

(C'') Tracks of non-junctional clusters for the conditions described in (C). Region shaded in grey outlines the EVL-YSL junction in yz direction; region shaded in pink outlines the internal YSL positioned animally from the EVL-YSL junction, where usually almost no cluster detachment is observed for ZO-1b, while for ZO-1b**Δ**ABR a substantial fraction (7%) of clusters detach (pink region);

region shaded in lilac shows clusters positioned further away from apical YSL surface, where many more ZO-1b**Δ**ABR than ZO-1b clusters were found (82% vs. 11%). ZO-1b with N=2, n=3 embryos; ZO-1b**Δ**ABR with N=3, n=3 embryos.

(D) MIPs of F-Actin (Phalloidin) of YSL-Ctrl (phenol red injected), *zo-1b/3* YSL-morphant (1.5 ng, 0.5 ng MO into the YSL) and *zo-1b/3* YSL-morphant embryos co-injected with GFP-tagged *zo-1b***Δ**C (15 pg) and *zo-3* (5 pg, mutated for MO recognition site) as well as GFP-tagged *zo-1b***Δ**ABR (22 pg) and *zo-3* (mutated) mRNAs at 8 hpf. Scale bar, 10 µm.

(D') Plot of F-Actin intensity as a function of distance from EVL margin for the conditions described in (D). YSL-Ctrl with N=2, n=6 embryos, *zo-1b/3* YSL-morphant with N=2, n=4 embryos, *zo-1b/3* YSL-morphant embryos co-injected with a combination of *zo-3* (5 pg, mutated for MO recognition site) and either GFP-tagged *zo-1b***Δ**C mRNA (15pg) with N=2, n=6 embryos or GFP-tagged *zo-1b***Δ**ABR mRNA (22 pg) with N=2, n=6 embryos. Statistical testing with Mann-Whitney test. Ctrl vs. *zo-1b/3* YSL-morphant with **p = 0.0095, Ctrl or *zo-1b/3* YSL-morphant vs. *zo-1b/3* YSL-morphant plus zo-3/*zo-1b***Δ**C mRNA with *p = 0.0152 and ns, respectively; Ctrl or *zo-1b/3* YSL-morphant vs. *zo-1b/3* YSL-morphant plus zo-3/*zo-1b***Δ**ABR mRNA with **p = 0.0022 and ns, respectively. ns, not significant.

(E) MIPs of GFP-tagged Claudin-D (30 pg) and mcherry-tagged ZO-1b (70 pg) localization at the EVL-YSL boundary at 8 hpf. Scale bar, 2µm.

(F) MIPs of mNEON-tagged Occludin-A (30-50 pg) and mcherry-tagged ZO-1b (70 pg) localization at the EVL-YSL boundary at 8 hpf. Scale bar, 2µm.

(G) MIPs of GFP-tagged ZO-1b (50 pg) and mcherry-tagged Cingulin-like 1 (50 pg) co-localization at the EVL-YSL boundary at 8 hpf. Scale bar, 2µm.

(G') Colocalization analysis (Pearson's R value) of GFP-tagged ZO-1b and mcherry-tagged Cingulin-like 1 in wild type (wt) embryos at 8 hpf. Pearson's R value = 0.8, indicating strong colocalization between the two proteins. N=3, n=9 embryos.

LEAD CONTACT AND MATERIALS AVAILABILITY

Further information and requests for resources, reagents, data, and code should be addressed to the Lead Contact, Carl-Philipp Heisenberg (heisenberg@ist.ac.at).

EXPERIMENTAL MODEL AND SUBJECT DETAILS

Zebrafish (Danio rerio) maintenance and embryo collection were carried out as described (Westerfield 2007). Embryos were raised at 25-31°C in E3 medium or Danieaus' buffer and staged as described (C. B. Kimmel et al. 1995). Embryos from TL or AB strains were used as wild type control embryos. Fish were bred in the zebrafish facility at IST Austria according to local regulations, and all procedures were approved by the Ethic Committee of IST Austria regulating animal care and usage.

METHOD DETAILS

CRISPR/Cas9 mutant generation

For target site determination of CRISPR/Cas9 mutants of *zo-1b (also known as tjp-1b, ZFIN ID: ZDB-GENE-070925-1)* and *zo-3* (also known as *tjp-3, ZFIN ID: ZDB-GENE-030828-10*) genes, the CHOPCHOP tool was used (http://chopchop.cbu.uib.no/index.php) (Labun et al. 2016; Montague et al. 2014). The following target sites were chosen: targeting exon number 13 (3rd PDZ domain) in *zo-1b* and '**g**(A)GCAAATGGGGACGCGGCAGTGG' targeting exon number 3 (1st PDZ domain) in *zo-3*. To increase the mutagenesis efficiency, the first (A) in the *zo-3* target site was mutated to a **g** (Gagnon et al. 2014)**.** To generate gRNA, a cloning-free method described in (Talbot and Amacher 2014) was used. Briefly, sgDNA templates were generated via PCR with the following general oligos: gRNA Primer 1: 5' - GCGTAATACGACTCACTATAG - 3', gRNA primer 2: 5' - AAAGCACCGACTCGGTGCCAC - 3' and sgDNA_rv: 5' - AAAAGCACCGACTCGGTGCCACTTTTTCAAGTTGATAACGGACTAGCCTTATTTTAACTTGCTATTTCTAGCTCT AAAAC - 3' and gene specific oligos: *zo-1b* oligo: 5' - GCGTAATACGACTCACTATAGTGGGCTTGAGGCTCGCTGGGTTTTAGAGCTAGAAATAGCAAG - 3' and *zo-3* oligo: 5' - GCGTAATACGACTCACTATA**g**GCAAATGGGGACGCGGCAGGTTTTAGAGCTAGAAATAGCAAG - 3'. Ambion MAXIscript T7 kit was used to transcribe sgRNA *in vitro*. sgRNA was co-injected with cas9 mRNA (transcribed from Addgene plasmid pCS2-Cas9 #47322 (Gagnon et al. 2014)) and a STOP cassette (GTCATGGCGTTTAAACCTTAATTAAGCTGTTGTAG flanked by 20nt homology arms). To determine indel frequencies, genomic DNA was prepared via HotSHOT protocol (Meeker et al. 2007) and the following primer pairs were used for identification of positive insertions of the STOP cassette: PCR of entire locus of *zo-1b* (5' - TGA AGG TGT TGA GAG AGA GCA G - 3' and 5' - CGTTTTTAGGACGTCTCTCACC - 3'), *zo-3* (5' - TTC TGT CTT TCA CAG GAT TCC A - 3' and 5' - CAT AAC AAT CTG ATC TCG CGT C - 3'); PCR of STOP cassette insertion site (5' - CATGGCGTTTAAACCTTAATTAAGCTGTTG - 3' in combination with gene-specific reverse primer; gene-specific forward primer in combination with 5' - CAACAGCTTAATTAAGGTTTAAACGCCATG - 3').

Finally, the following mutations in *zo-1b* and *zo-3* mutants were identified:
zo-1b mutant (#14): 462 aa before STOP codon (*)
…APVPSVTHDDSILRPSMKLVKFKKGESVGLRHDV*
zo-3 mutant (#13): 44 aa before STOP codon (*)
MEEMTIWEQHTVTLSKDSKVGFGFAVSGGLDKPNPANGDAGHGV*

Frequently, we observed smaller egg sizes in the case of MZ*zo-1b* single mutants and sometimes also in the MZ*zo-1b/3* double mutants. For quantification of EVL epiboly movement in those mutants, we thus only used wild type eggs with similar sizes as controls.

While we were able to rescue the *zo-1b/3* morphant phenotype by co-injection of *zo-1b* and *zo-3* mRNA, attempts to rescue the MZ*zo-1b/3* mutant phenotype by *zo-1b* and *zo-3* mRNA injection frequently resulted in gain-of-function phenotypes, reflected by ectopic constriction of the yolk cell by the circumferential actomyosin ring within the YSL. This difference in the efficiency of rescuing the morphant compared to the mutant phenotype might be due to difficulties in achieving the right level of expression in the mutant but not the morphant required for a successful rescue. This could be due to the upregulation of other *zo* genes in mutants (Figure S2H) but not morphants as a result of potential nonsense-mediated decay (El-Brolosy et al. 2019).

Cloning of expression constructs

Wild type TL or Tuebingen embryos were collected at 4 hpf or 8 hpf, dechorionated and total RNA was extracted from 10-15 embryos per sample using Trizol (Invitrogen). cDNA library was generated with the Superscript III reverse transcription kit according to manufacturer's instructions. Coding region of zebrafish ZO-1b (splice variant: ENSDART00000112588.5), ZO-3 (splice variant: ENSDART00000012336.10) and Cingulin-like 1 (splice variant: ENSDART00000129769.4) were cloned with following primers: *zo-1b* (5' - GGGG ACA AGT TTG TAC AAA AAA GCA GGC TTC ATG TCT GCC CGG GCT GC - 3' and 5' - GGG GAC CAC TTT GTA CAA GAA AGC TGG GTC TCA GAA GTG GTC GAT CAG CAC - 3'), *zo-3* (5' - GGGG ACA AGT TTG TAC AAA AAA GCA GGC TTC ATG GAG GAG ATG ACG ATA TGG G - 3' and 5' - GGG GAC CAC TTT GTA CAA GAA AGC TGG GTC TTA CAG CTC TGT AGC AGG TCC - 3') and *cingulin-like 1 (*5' - GGGG ACA AGT TTG TAC AAA AAA GCA GGC TTA ATG GAG TCG TAC AGA GT TGG T - 3' and 5' - GGG GAC CAC TTT GTA CAA GAA AGC TGG GTA TCA CAT TGA GAA ACT GGA GAT - 3').

Occludin-A was cloned from 5604348 (IMAGE ID) cDNA clone ordered from Source BioScience with following primers: *oclnA* (5' - GGGG ACA AGT TTG TAC AAA AAA GCA GGC TTC ATG TCG TCG AAG CAC ATC GG - 3' and 5' - GGG GAC CAC TTT GTA CAA GAA AGC TGG GTC GGA TCT GCG GTC GTA ATC GC - 3').

PCR products were used to generate entry vectors via recombining with pDONR(P1-P2) (Lawson#208) and the entry clone was further recombined with pCS-N-term-EGFP (Lawson #223) or pCS-N-term-mCherry (Lawson #362) destination vector (*zo-1b*, *zo-3*, *cingulin-like1*) or p3E mNEONgreen, pCS2-Dest (Lawson #444) for C-terminal tagging (*occludin-A*).

For morphant rescue experiments, a slightly shorter transcript of *zo-1b* was expressed (splice variant: ENSDART00000112588.5) that is not targeted by the MO. For *zo-3* morphant rescue, four mutations were introduced into the MO recognition site of *zo-3* (pCS2-*GFP-zo-3_4mismatch*): 5' - GAa GAG ATG ACc ATt TGG GAa CAG CAC ACG -3'.

To obtain the different *zo-1b* deletion constructs, the following primers were used to generate different truncated constructs: GFP-ZO-1b-ΔC (5' - **TGA** GAC CCA GCT TTC TTG TAC AAA G - 3' and 5' - AAT GAC TGG CGG GTC CTC TCG C - 3'), GFP-ZO-1b-ΔABR (5' - AGC GCT GGA GTA AAC CGC TTC - 3' and 5' - AGG TTT GGG GTG CCG CGG - 3').

The desired truncations were amplified with PCR, followed by DpnI digest to remove template DNA (methylated DNA). T4 Polynucleotide kinase kit (NEB) was used for 5' phosphorylation of DNA for subsequent ligation with T4 ligase kit (NEB). Transformation was performed in One Shot™ TOP10 Chemically Competent E. coli (Thermo Fisher Scientific).

Transgenic zebrafish line generation

The Tol2/Gateway technology was used to generate transgenic fish lines (Kwan, Fujimoto, and Grabher 2007; Villefranc, Amigo, and Lawson 2007). For ZO-1b, ZO-1b-ΔABR flow imaging and FRAPs, lines ubiquitously expressing mNEONgreen-tagged ZO-1b and ZO-1bΔABR were generated. The following primers with gateway arms were used to amplify the coding region of *zo-1b*

(ENSDART00000112588.5) from a cDNA library of wild type TL embryos at 8 hpf or from *zo-1b-ΔABR* template plasmid:
5‘ - GGGGACAGCTTTCTTGTACAAAGTGGCTATGTCTGCCCGGGCTGCCTCTAAT - 3’
5’ - GGGGACAACTTTGTATAATAAAGTTGCTCAGAAGTGGTCGATCAGCACAGAC - 3’.
PCR products were used to generate entry vectors via recombing with pDONRP2r-P3 (Lawson#211) and entry clones were further recombined with pDestTol2pA2 (Chien #394), p5E-β-actin promoter (Chien#229), pME mNeonGreen (Shaner et al. 2013) (mNeonGreen licensed by Allelebiotech) and p3E-polyA (Chien#302). Transposase mRNA (Invitrogen) along with the Tol2 construct were co-injected into wild type embryos (TL strain) to generate Tg(*actb2:mNEONgreen-zo-1b*) transgenic line. To generate the transgenic lines MZ*zo-1b/3*;Tg(*actb2:mNeonGreen-zo-1b*) and MZ*zo-1b/3*; Tg(*actb2:mNeonGreen-zo-1bΔABR*), the respective constructs were co-injected with transposase mRNA into MZ*zo-1b/3* mutant embryos.

Tg(*actb1:myl12.1-mcherry*;*actb2:mNEONgreen-zo-1b*) and Tg*(actb2:mNeonGreen-zo-1b; actb1:Utrophin-mcherry)* transgenic lines were generated by crossing Tg(*actb2:mNEONgreen-zo-1b*) with pre-existing Tg(*actb1:myl12.1-mcherry)* or Tg*(actb1:Utrophin-mcherry)* lines, respectively.
Other transgenic lines used were Tg(*actb1:myl12.1-eGFP*) and Tg(*actb1:myl12.1-mcherry*) (Maître et al. 2012; Behrndt et al. 2012) to follow cortical flow rates and perform laser cuts, and Tg(*actb2:Lyn-TdTomato*) (Compagnon et al. 2014) to label cell membranes for tracking EVL margin progression.

mRNA and Morpholino injections
mRNA transcription was performed using the SP6 mMessage mMachine Kit (Ambion). Glass capillaries (30-0020, Harvard Apparatus) were pulled using a needle puller (P-97, Sutter Instruments) and mounted on a microinjection system (PV820, World Precision Instruments). Injections at one-cell stage were performed as described (Westerfield 2007). YSL injections were performed at high stage (3.3 hpf). 0.2% Phenol red was co-injected as control. For caRhoA overexpression experiments, we locally increased actomyosin contraction within the YSL by injecting a single marginal blastomere at 128-cell stage, because global YSL expression of caRhoA resulted in premature constriction of the actomyosin band, and consequently in embryo lysis. The following mRNAs were injected: *membrane-RFP* (Iioka, Ueno, and Kinoshita 2004), *membrane-GFP (R. A. Kimmel and Meyer 2010)*, *lifeact-RFP* (Behrndt et al. 2012) to label cell membranes and cortical actin for tracking EVL margin progression, *H2A-mCherry* (Arboleda-Estudillo et al. 2010) and *H2B-GFP* (Keller et al. 2008) to mark the YSL injection sites by locally labelling nuclei. Concentration of mRNAs are specified in the individual figure legends.

The following Morpholino (MO) sequences were used to generate translation initiation MO: *zo-1b* (ENSDART00000173656.2 - longest variant): 5’ - GTCCGCCAAAGACAGACAAGAGCAT -3’; *zo-3* (ENSDART00000012336.10 - longest variant, ENSDART00000147070.3, ENSDART00000139911.2): 5’ - GCTCCCATATCGTCATCTCCTCCAT - 3’. Titration curves with different *zo-1b/3* MO concentrations and different amounts of *zo-1b/3* mRNAs were performed to find a dose of MOs, which induces phenotypes that can be rescued. This dose (1.5 ng *zo-1b* MO and 0.5 ng *zo-3* MO) was then injected into MZ*zo-1b/3* mutants at one-cell stage to exclude that additional (potentially unspecific) phenotypes are induced. As further controls, 5-base mismatch control MOs (*zo-1b* 5-base mismatch MO 5’ - GTgCGgCAAAGAgAcACAAcAGCAT - 3; *zo-3* 5-base mismatch MO 5’ - GgTCgCATATCcTCATCTCgTCgAT - 3’) and a standard negative control MO (human beta-globin MO 5’ - ‘CCTCTTACCTCAGTTACAATTTATA’ - 3’, Gene Tools) were used.

Sample preparation for live imaging
Embryos were dechorionated and mounted in 0.3-0.5% low melting point (LMP) agarose (Invitrogen) for live imaging on glass bottom dishes (MatTek). Fixed samples were mounted in 0.5-1% LMP

agarose and put into prepared agarose moulds (2%) for upright imaging. Live embryos were imaged at 28.5°C ± 1°C.

Imaging setups for live and fixed imaging

For live imaging, Leica SP5 inverted microscope equipped with a 20x/0.7 CS objective. (HC PL APO, 11506513 WD=0.59 mm, D=0.17 mm) was used. For imaging fixed samples, Leica SP5 inverted microscope equipped with a 40x objective (HCX PL APO 40x/1.25-0.75 OIL CS - 11506251, WD=0.1 mm, D=0.17 mm) or Leica SP5 upright equipped with a 25x/0.95 W dipping lense (HCX IRAPO L, 11506323, WD=2.5 mm) were used.

Analysis of EVL progression

To determine EVL progression throughout development, the height of EVL (h_{EVL}) was normalized to the total embryo height (h_{TOT}), and then normalized to the average time needed by control embryos and plotted as a function of time. In general, the interval time was set by the acquisition time (10 min); in case of different acquisition times, the EVL progression was interpolated to gain intervals of 10 min. Data of Figure 6D-D',E-E' were randomized before quantification of total EVL epiboly duration.

Whole mount in situ hybridization

Embryos at 10.5 hpf were fixed in 4% PFA and then dehydrated and stored for at least 1 day at -20°C. Following rehydration in 1xPBS, *in situ* hybridization was performed as previously described (Montero et al. 2005). Antisense RNA probe for *papc* was synthesized from partial cDNA sequence via mMESSAGE mMACHINE™ T7 Transcription Kit (ThermoFisher AM1344) and DIG-RNA labeling mix (Sigma, 11 277 073 910). A stereomicroscope (Olympus SZX 12) equipped with QImaging Micropublisher 5.0 camera was used to take images of whole mount embryos.

UV laser ablation

Inverted Zeiss microscope (Axio Observer Z1) equipped with a 355 nm UV-A laser and a 63x/1.2 W objective (Korr UV-VIS-IR, 421787-9970) was used to assess junctional tension (Behrndt et al. 2012). Junctional cuts were performed on Tg(*actb1:myl12.1-eGFP*) (Maître et al. 2012) embryos by cutting at 10 equidistant sites along a 5 µm line perpendicular to the junction with 25 UV pulses at 1 kHz. Time for junctional laser ablation was 300-350 msec and for subsequent imaging 300 msec. For determining recoil velocities, first the movement of the junction was corrected (via stackreg function in ImageJ), and a line was drawn along the junction, including the position of ablation to generate a kymograph. The kymograph was then used to extract the opening distance after junctional ablation. A linear fit was performed on the first 4 post-cut distances when plotting distance (in µm) versus time (in s) (see Fig S2I-I',J-J'). Cases where a wound response after UV cutting was detected were excluded from the quantification.

Imaging of cortical flows within the YSL

For imaging cortical flows of Myosin-2, Tg(*actb1:myl12.1-eGFP*) (Maître et al. 2012) embryos were used, and for simultaneously monitoring ZO-1b and Myosin-2 flows, Tg(*actb1:myl12.1-mcherry*; *actb2:mNEONgreen-zo-1b*) embryos were used. High-resolution confocal imaging was performed on a spinning disk setup (Axio Observer Z1, Zeiss) equipped with 100x/1.4 Oil/DIC (Plan APOCHROMAT, 420792-9900). Z-stacks of 5-10 µm (0.5 µm in z) were acquired by recording multiple positions along the animal-vegetal (AV) axis of the YSL within the same embryo at a maximum acquisition time of 15 sec. Afterwards, the different positions were stitched via ImageJ plugin (Preibisch, Saalfeld, and Tomancak 2009). Particle image velocimetry (PIV) analysis on maximum intensity projections was performed by using PIVlab in matlab after applying a CLAHE filter (Contrast Limited Adaptive Histogram Equalization) to enhance the local contrast of the images. In order to gain mean flow profiles along the AV axis, the linear EVL movement was corrected in order to keep the EVL margin

fixed at position 0. From these plots, the peak EVL and YSL flow velocities were extracted to determine whether flow rates had changed in the different conditions. Movies lasted for 5-30 min.

ZO-1b cluster size and circularity analysis

For high spatiotemporal resolution imaging of non-junctional ZO-1b clusters within the YSL, an Axio Observer Z1 inverted microscope (Zeiss, LSM880) equipped with Plan-Apochromat 63x / NA 1.4 Oil was used. For determining the average cluster area, a maximum intensity projection (MIP) was performed and the movement of the junction was corrected (via stackreg function in ImageJ). Images were further processed using Ilastik (Sommer et al. 2011) to train the program for properly detecting signal intensities versus background signal. After cluster segmentation, the average cluster area size over time was determined. Circularity was determined via using the plugin 'Circularity' in Fiji, which calculates circularity as

$$\text{Circularity} = 4\pi * \frac{area}{perimeter^2}. \qquad \text{Equation (1)}$$

A circularity value of 1 reflects a perfect circle, while values close to 0 indicate more elongated shapes.

ZO-1b cluster fusion analysis

For analyzing the cluster fusion rate, the FiJi plugin TrackMate, and specifically the 'FindMaxima' detector, was used to identify and track bright clusters on MIP images. From the tracking information, the cluster fusion events per time point were then extracted using a custom-made Python script.

Quantitative imaging of ZO-1b

Axio Observer Z1 inverted microscope (Zeiss, LSM880) equipped with Plan-Apochromat 63x / NA 1.4 Oil in Airy Scan mode was used for obtaining GFP calibration curves to determine ZO-1b concentrations. Before each experiment, the Argon laser power was measured with a power meter to normalize to potential fluctuations. For obtaining GFP calibration curves, Matek dishes were coated in 1% BSA for 2h at RT and washed several times before addition of a GFP solution with known concentration. GFP protein solutions were diluted in 1xPBS. Three images per GFP dilution were acquired and averaged. Finally, fluorescence intensity of GFP protein dilutions were plotted against protein concentration (Figure S5A) and the resulting equation of the linear relationship was used to convert fluorescence intensity to ZO-1b protein concentration in µM.

ZO-1b junctional integration efficiency

Non-junctional clusters of ZO-1b were manually tracked in maximum intensity projection images (MIP) using FIJI after EVL-YSL junctional movement correction (via stackreg function in ImageJ). The junctional integration efficiency was calculated as described in Figure S6B.

Tracking analysis of non-junctional clusters

For 3D tracking of non-junctional clusters of ZO-1b and ZO-1bΔABR (Figure S6C-C''), the EVL movement was corrected in order to keep the EVL margin fixed at position 0 via the plugin 'correct 3D drift' in FIJI. Then, Imaris tracking 'spots' tool was used. Tracks in yz planes were extracted and a custom-made Matlab script was used to plot single tracks in yz axes. The percentages of tracks that bypassed the junction in z (lilac box) and tracks that detached from the junction (pink box) were calculated and indicated within the boxes.

Immunostaining

Immunostaining was performed as described (Köppen et al. 2006). Briefly, embryos were fixed in 4% paraformaldehyde overnight at 4 °C. For ZO-1 and ZO-3 immunohistochemistry, fixed embryos were washed in 0.1% Triton X-100 (in PBS) and dechorionated. After another washing step embryos were permeabilized in 0.5% Triton X-100 for 1h and blocking was performed in blocking solution (10% normal goat serum, 1% DMSO, 0.3% Triton in PBS) for 3-5h at room temperature (RT). Embryos were incubated with primary antibodies in blocking solution overnight at 4 °C. Primary antibodies used were mouse anti-ZO-1 (Invitrogen) at 1:50, and rabbit anti-ZO-3 (Benais-Pont et al. 2003) (gift from Karl Matter) at 1:300. After washing the embryos in 0.1% Triton in PBS, they were incubated for 3-4h in secondary antibody solutions at RT or at 4 °C overnight and washed again before imaging.

For E-Cadherin, α- and β-Catenin staining, embryos were dehydrated after fixation and stored in 100% Methanol at -20 °C overnight. After rehydration, embryos were washed in PBS and incubated in 0.5% Triton X-100 for 1h and blocking was performed in blocking solution (0.5% Tween-20, 0.5% Triton X-100, 1% DMSO, 1% BSA in PBS) for 3-5 h at RT. Embryos were incubated with primary antibodies (rabbit anti - zebrafish E-Cadherin, 1:200, generated at MPI-CBG; rabbit α-Catenin 1:1000, Sigma; mouse anti-β-Catenin, 1:500, Sigma) in blocking solution at 4 °C overnight. Embryos were washed 4x 20 min in blocking buffer and then incubated with secondary antibodies in blocking solution for 3-5 h at RT. Secondary antibodies used were goat anti-mouse/rabbit conjugated to Alexa Fluor 488/594/647 (Molecular probes). To label F-Actin, Phalloidin conjugated to Alexa Fluor 488/Rhodamine/647 was added to the secondary antibody solutions. Finally, embryos were washed 4x 20 min in 0.5% Tween in PBS.

Junctional and YSL cortical quantifications

For quantification of junctional intensities of immunostained embryos, z-stack planes were summed via SUM projection (in ImageJ), and of GFP-tagged and mNEONgreen-tagged protein expression constructs (Cingulin-like 1, Claudin-D, Occludin-A, ZO-1b, ZO-1b-ΔC and ZO-1b-ΔABR), maximum intensity projection was performed. A 1 µm segmented line was then drawn along EVL-YSL and EVL-EVL junctions to measure mean fluorescence intensity. For cytoplasmic signal intensities a window of around 5x5 µm was analyzed. For quantification of non-junctional intensities of YSL cortical signals, a mask of the YSL region was generated and average intensity values along the distance to the EVL were extracted after background subtraction.

Quantification of total intensities

GFP-tagged constructs were injected into MZ*zo-1b/3* embryos and z-stack planes were summed via SUM projection (in ImageJ) over a 10 µm thickness. A 70 µm x 70 µm window was selected and total intensity was normalized to the used laser power.

qRT-PCR (quantitative Real-Time PCR)

Wild type TL and MZ*zo-1b/3* embryos were collected at 6 hpf, dechorionated and total RNA was extracted from 10-15 embryos per sample using Trizol (Invitrogen). To ensure complete removal of any contaminating genomic DNA, DNA-free™ DNA Removal Kit (Thermo Fisher Scientific) was used. cDNA library was generated with the Superscript III reverse transcription kit according to manufacturer's instructions. Equal amounts of mRNA were used from different samples for the actual qRT-PCR experiment. Experiments were repeated 3 times independently in triplicates. Absolute QPCR SYBR Green Mixes (Thermo Scientific) and Bio-Rad C1000 Thermal Cycler was used for qRT-PCR reaction. As negative control, cDNA library generation was performed without adding the reverse transcriptase. As positive control and for later normalization, the housekeeping gene *elongation factor 1α* (Miesfeld et al. 2015) was used. To determine the linear range, different concentrations of cDNA concentrations were tested to finally use a 1:10 cDNA dilution. Primers were used at a final concentration of 105 nM: *zo-1b* (5' - CAACAACATCAACGCCATTC - 3' and 5' - CCACAACTGTGTGTCCCTCA - 3'), *zo-3* (5' - ACCTGGAGGAACCCTTAGGA - 3' and 5' -

TGTAGGGAGGTTCAGGGCTA - 3'), *zo-1a* (5' - CCAGCTACAACCGTTTTGTG - 3' and 5' - TTGGGAGTCATTAGGGAGGA - 3'), *zo-2a* (5' - CATCATACCCAGCAAGAGCA - 3' and 5' - CTCCAGAAATCGCCTCTGTC - 3') and *zo-2b* (5' - GATTACCGCAGCCAGGACTA - 3' and 5' - GTCCCTCCGGTACCCACT - 3').

Colocalization analysis

Images for colocalization analysis of ZO-1b and Myosin-2 were acquired on a Zeiss LSM880 inverted microscope (Airyscan mode, Plan-Apochromat 63x / NA 1.4 Oil) using Tg(*actb1:myl12.1-mcherry*; *actb2:mNEONgreen-zo-1b*) embryos at 6-8 hpf and colocalization of cingulin-like 1 and ZO-1b images were acquired by injecting mcherry and GFP-tagged versions into wild type embryos at 8 hpf. After determining the point spread function and the chromatic shift between channels (via imaging TetraSpeck Microspheres with the size of 100 nm), the mcherry channel was corrected for chromatic shift using DoM 'Detection of Molecules' plugin in ImageJ, and images were analyzed by using 'Coloc2' plugin in ImageJ. As a quantitative measure for colocalization analysis of ZO-1b and Myosin-2, Li's Intensity Correlation Quotient (Li's ICQ) was determined, best suited for the rather complex and heterogeneous distribution of channel intensities in our samples (also see scatter-plot in Figure S5B') (Q. Li et al. 2004; Bolte and Cordelières 2006). Li's ICQ value ranges from 0.5 showing colocalization to -0.5 showing exclusion with values close to 0 indicate random localization. As a quantitative measure for colocalization between Cingulin-like 1 and ZO-1b, Pearson's R value was determined by using 'Coloc2' plugin in ImageJ, which was best suited for the observed linear relationship between the two protein species (also see scatter-plot in Figure S6G') (Bolte and Cordelières 2006).

Fluorescence Recovery After Photobleaching

Data acquisition

Fluorescence Recovery After Photobleaching (FRAP) experiments were performed on a Spinning Disk System (Andor, iXon 897, backthinned EMCCD) assembled on an Axio Observer Z1 microscope (Zeiss) equipped with a 40x/1.2 W objective (C-APOCHROMAT, Korr UV-VIS-IR). Three pre-bleach frames were acquired for estimating the level of bleaching followed by bleaching a 5x5 µm window with a 488 nm laser. For bleaching, a dwell time of 20-60µs and 5-30x repeats at laser powers of 9-15% was used. Several junctions within the field of view were bleached, but only one junction per cell. Due to the continuous movement of the EVL-YSL junction, a 10µm z-stack was imaged with an acquisition time of 10 sec.

Data analysis

For FRAP analysis at the EVL-YSL boundary, sum intensity projection was performed on z-stacks of the EVL-YSL junction. The ImageJ plugin 'stackreg with rigid body transformation' was used to correct for movement of the junction and to keep the FRAP window at a constant position. Then, a 1 µm thick line was drawn along the junction and the signal along the thickness of the line was averaged via the 'KymoResliceWide' function. Finally, a 5 µm thick line was used to measure the intensities before and after bleaching on the generated kymograph (see white dashed box in Figure S4A-A',B-B').

Background (BG) subtraction was performed by measuring signal outside of the junctional region of the pre-bleach frame (I_{BG}) to obtain the background corrected intensity at the EVL-YSL junction ($I_{J\text{-}BGcorr}$) and at the reference EVL-EVL junctions ($I_{Ref\text{-}BGcorr}$).

$$I_{J\text{-}BGcorr}(t) = I_{J}(t) - I_{BG} \qquad \text{Equation (2)}$$

$$I_{Ref\text{-}BGcorr}(t) = I_{Ref}(t) - I_{BG} \qquad \text{Equation (3)}$$

Next, to obtain the intensity corrected for bleaching ($I_{J\text{-}BLcorr}$), the intensity of junctional signal was divided by a reference signal (average of two EVL-EVL junctions):

$$I_{J\text{-}BLcorr}(t) = I_{J\text{-}BGcorr}(t) / I_{Ref\text{-}BGcorr}(t) \quad \text{Equation (4)}$$

The bleach corrected intensity was then normalized to the mean pre-bleach intensity (average of three pre-bleach frames, N=3):

$$I_{J\text{-}norm}(t) = \frac{1}{N}\sum_{N} I_{J\text{-}BLcorr}(t) \quad \text{Equation (5)}$$

For the analysis of non-junctional FRAPs, initial data analysis was carried out as described for junctional FRAPs. A 5 µm thick line was drawn along the non-junctional pool and the signal along the thickness of the line was averaged via the 'KymoResliceWide' function. Finally, a 5µm thick line was used to measure the intensities before and after bleaching on the generated kymograph (see white dashed box in Figure 4E-E',F-F'). Background subtraction was carried out as described for junctional FRAPs - Equation (2,3). Then, the background corrected intensities of the non-junctional signal ($I_{nJ\text{-}BGcorr}(t)$) and the reference signal ($I_{Ref\text{-}BGcorr}(t)$) were normalized to three pre-bleach frames.

$$I_{nJ\text{-}norm}(t) = \frac{1}{N}\sum_{N} I_{nJ\text{-}BGcorr}(t) \quad \text{Equation (6)}$$

$$I_{Ref\text{-}norm}(t) = \frac{1}{N}\sum_{N} I_{Ref\text{-}BGcorr}(t) \quad \text{Equation (7)}$$

Finally, the change in signal of the reference region (unbleached non-junctional region) was deducted from the non-junctional intensity measurements to account for retrograde flow that would otherwise also contribute to signal recovery within the bleached window:

$$I_{nJ\text{-}norm;corr}(t) = I_{nJ\text{-}norm}(t) - [\, I_{Ref\text{-}norm}(t) - 1] \quad \text{Equation (8)}$$

Latrunculin B treatment

Dechorionated embryos were mounted in 0.5% low melting point agarose containing 1 ug/ml Latrunculin B or DMSO as control at the onset of epiboly (4.3 hpf). Danieau's medium containing 1ug/ml Latrunculin B (EMD Millipore) or DMSO (Sigma) was then added. After a 1h incubation period, embryos were imaged with Axio Observer Z1 inverted microscope (Zeiss, LSM880) equipped with Plan-Apochromat 63x / NA 1.4 Oil in Airy Scan mode at 5.3 till 6.3 hpf.

QUANTIFICATION AND STATISTICAL ANALYSES

Graphpad Prism 6 was used for statistical analysis. All data were tested for normal distribution with 'D'Agostino & Pearson omnibus normality test'. In case data passed normality test (alpha=0.05), then a parametric test, such as unpaired t test or ordinary one-way ANOVA (in the case of multiple comparisons) was used. In case the data did not pass the normality test, a non-parametric test was used (Mann-Whitney test or Kruskal-Wallis test for multiple comparisons). To correct for multiple comparisons either Tukey's multiple comparisons test (for ordinary one-way ANOVA) or Dunn's multiple comarisons test (for Kruskal-Wallis test) was used. The individual statistical tests used for experiments are mentioned in the according figure legends. In general, N were considered as independent experiments and n were determined either as number of embryos or number of cells, which is specified in the individual figure legends.

DATA AND CODE AVAILABILITY

All data and code supporting the current study are available from the corresponding author upon request.

Supplemental Videos:

Video S1: *zo-1b/3* function is specifically required within the YSL to ensure proper EVL epiboly. Related to Figure 2.
Time-lapse brightfield/fluorescence movie of embryos labeled with membrane RFP to detect EVL and deep cells of exemplary embryos for control YSL-injected, *zo-1b/3* MO YSL-injected, and *zo-1b/3* MO together with GFP-tagged *zo-1b and zo-3* mRNA YSL-injected conditions. EVL-YSL boundary is marked by white dashed line to demarcate extent of EVL epiboly in the different conditions.Time-interval: 10 min. Time: 4-11 hpf. Scale bar: 100 µm.

Video S2: *zo-1b/3* regulate actomyosin flow rates within the YSL. Related to Figure 2.
Time-lapse movie of maximum intensity projections (MIPs) of myosin-2 flow during epiboly in an exemplary YSL-Ctrl (left panel), *zo-1b/3* YSL-morphant embryo (middle panel) and *zo-1b/3* YSL-morphant embryo rescued with GFP-*zo-1b/3* mRNA (right panel) at 7-8 hpf. Fluorescent signal of myosin-2 (left side) was overlaid with vectors (in green - right side) obtained by PIV analysis to indicate the flow velocities along the animal-vegetal (AV) axis of the embryo. Time-interval: 15 sec. Scale bar: 10 µm.

Video S3: Non-junctional ZO-1b flows with similar velocity as cortical actomyosin. Related to Figure 4.
Time-lapse movie of maximum intensity projections (MIPs) of myosin-2 (left panel) and ZO-1b (right panel) flow in Tg(*actb1:myl12.1-mcherry*; *actb1:mNEONgreen-zo-1b*) embryos at 7-8 hpf. Fluorescence signal of myosin-2 and ZO-1b (left side) were overlaid with vectors (in green - right side) obtained by PIV analysis to indicate the flow velocities along the animal-vegetal (AV) axis of the embryo. Time-interval: 15 sec time. Scale bar: 10 µm.

Video S4: Non-junctional ZO-1b clusters fuse within YSL. Related to Figure 4.
Time-lapse movie of maximum intensity projections (MIPs) of high-resolution (Airy Scan) images of non-junctional ZO-1b clusters undergoing fusion close to the EVL-YSL boundary in a Tg(*actb1:mNEONgreen-zo-1b*) embryo at 6.5-8 hpf. To keep the non-junctional pool at a constant position, correction for EVL-YSL movement was performed. Time-interval: 20 sec. Scale bar: 1 µm.

Video S5: Fusion of non-junctional ZO-1b clusters occurs independently of actomyosin network contraction. Related to Figure 5.
Time-lapse movie of maximum intensity projections (MIPs) of high-resolution (Airy Scan) images of non-junctional ZO-1b clusters undergoing fusion in Tg(*actb1:mNEONgreen-zo-1b*) embryos treated for 1h with DMSO (left panel) or 1 µg/ml Latrunculin B (Lat B, right panel) prior to imaging at 5.3-6.3 hpf. To keep the non-junctional pool at a constant position, correction for EVL-YSL movement was performed. Red arrowheads mark fusing ZO-1b droplets (right panel). Time-interval: 15 sec. Scale bar, 2 µm.

Video S6: ZO-1b-ΔABR clusters show decreased junctional integration efficiency. Related to Figure 6.
Time-lapse movie of maximum intensity projections (MIPs) of ZO-1b (left panel) and ZO-1b-ΔABR (right panel) non-junctional pool in MZ*zo-1b/3* mutant embryos injected with either GFP-*zo-1b* (50pg) or GFP-*zo-1bΔABR* (44pg) mRNA at 7-8 hpf. To keep the junction at a constant position, correction for EVL-YSL movement was performed. Black arrowheads point at clusters of ZO-1b that get successfully incorporated into the EVL-YSL junction (left panel), while non-junctional clusters of ZO-1b-ΔABR frequently bypass the junction (right panel). Time-interval: 15 sec. Scale bar: 2 µm.

References

Alberti, Simon. 2017. “Phase Separation in Biology.” *Current Biology: CB* 27 (20): R1097–1102.

Arboleda-Estudillo, Yohanna, Michael Krieg, Jan Stühmer, Nicholas A. Licata, Daniel J. Muller, and Carl-Philipp Heisenberg. 2010. “Movement Directionality in Collective Migration of Germ Layer Progenitors.” *Current Biology: CB* 20 (2): 161–69.

Banani, Salman F., Hyun O. Lee, Anthony A. Hyman, and Michael K. Rosen. 2017. “Biomolecular Condensates: Organizers of Cellular Biochemistry.” *Nature Reviews. Molecular Cell Biology* 18 (5): 285–98.

Bauer, H., J. Zweimueller-Mayer, P. Steinbacher, A. Lametschwandtner, and H. C. Bauer. 2010. “The Dual Role of Zonula Occludens (ZO) Proteins.” *BioMed Research International* 2010. http://downloads.hindawi.com/journals/biomed/2010/402593.pdf.

Baum, Buzz, and Marios Georgiou. 2011. “Dynamics of Adherens Junctions in Epithelial Establishment, Maintenance, and Remodeling.” *The Journal of Cell Biology* 192 (6): 907–17.

Behrndt, Martin, Guillaume Salbreux, Pedro Campinho, Robert Hauschild, Felix Oswald, Julia Roensch, Stephan W. Grill, and Carl-Philipp Heisenberg. 2012. “Forces Driving Epithelial Spreading in Zebrafish Gastrulation.” *Science* 338 (6104): 257–60.

Benais-Pont, Gaëlle, Anu Punn, Catalina Flores-Maldonado, Judith Eckert, Graça Raposo, Tom P. Fleming, Marcelino Cereijido, Maria S. Balda, and Karl Matter. 2003. “Identification of a Tight Junction–associated Guanine Nucleotide Exchange Factor That Activates Rho and Regulates Paracellular Permeability.” *The Journal of Cell Biology* 160 (5): 729–40.

Beutel, Oliver, Riccardo Maraspini, Karina Pombo-Garcia, Cécilie Martin-Lemaitre, and Alf Honigmann. n.d. “Phase Separation of Zonula Occludens Proteins Drives Formation of Tight Junctions.” https://doi.org/10.1101/589580.

Bolte, S., and F. P. Cordelières. 2006. “A Guided Tour into Subcellular Colocalization Analysis in Light Microscopy.” *Journal of Microscopy* 224 (Pt 3): 213–32.

Brangwynne, Clifford P., Christian R. Eckmann, David S. Courson, Agata Rybarska, Carsten Hoege, Jöbin Gharakhani, Frank Jülicher, and Anthony A. Hyman. 2009. “Germline P Granules Are Liquid Droplets That Localize by Controlled Dissolution/condensation.” *Science* 324 (5935): 1729–32.

Bruce, Ashley E. E. 2016. “Zebrafish Epiboly: Spreading Thin over the Yolk.” *Developmental Dynamics: An Official Publication of the American Association of Anatomists* 245 (3): 244–58.

Cavey, Matthieu, Matteo Rauzi, Pierre-François Lenne, and Thomas Lecuit. 2008. “A Two-Tiered Mechanism for Stabilization and Immobilization of E-Cadherin.” *Nature* 453 (7196): 751–56.

Cavey, M., and T. Lecuit. 2009. “Molecular Bases of Cell–cell Junctions Stability and Dynamics.” *Cold Spring Harbor Perspectives in*. http://cshperspectives.cshlp.org/content/early/2009/08/31/cshperspect.a002998.abstract.

Cheng, Jackie C., Andrew L. Miller, and Sarah E. Webb. 2004. “Organization and Function of Microfilaments during Late Epiboly in Zebrafish Embryos.” *Developmental Dynamics: An Official Publication of the American Association of Anatomists* 231 (2): 313–23.

Christensen, Rune Haubo B. 2018. “Cumulative Link Models for Ordinal Regression with the R Package Ordinal.” *Submitted in J. Stat. Software*. http://cran.uni-muenster.de/web/packages/ordinal/vignettes/clm_article.pdf.

Citi, Sandra, Pamela Pulimeno, and Serge Paschoud. 2012. “Cingulin, Paracingulin, and PLEKHA7: Signaling and Cytoskeletal Adaptors at the Apical Junctional Complex.” *Annals of the New York Academy of Sciences* 1257 (June): 125–32.

Compagnon, Julien, Vanessa Barone, Srivarsha Rajshekar, Rita Kottmeier, Kornelija Pranjic-Ferscha, Martin Behrndt, and Carl-Philipp Heisenberg. 2014. “The Notochord Breaks Bilateral Symmetry by Controlling Cell Shapes in the Zebrafish Laterality Organ.” *Developmental Cell* 31 (6): 774–83.

Cunningham, Kevin E., and Jerrold R. Turner. 2012. “Myosin Light Chain Kinase: Pulling the Strings of Epithelial Tight Junction Function.” *Annals of the New York Academy of Sciences* 1258 (July): 34–42.

El-Brolosy, Mohamed A., Zacharias Kontarakis, Andrea Rossi, Carsten Kuenne, Stefan Günther, Nana Fukuda, Khrievono Kikhi, et al. 2019. “Genetic Compensation Triggered by Mutant mRNA Degradation.” *Nature* 568 (7751): 193–97.

Engl, W., B. Arasi, L. L. Yap, J. P. Thiery, and V. Viasnoff. 2014. “Actin Dynamics Modulate Mechanosensitive Immobilization of E-Cadherin at Adherens Junctions.” *Nature Cell Biology* 16 (6): 587–94.

Fanning, Alan S., and James M. Anderson. 2009. “Zonula Occludens-1 and-2 Are Cytosolic Scaffolds That Regulate the Assembly of Cellular Junctions.” *Annals of the New York Academy of Sciences* 1165 (1): 113–20.

Fanning, Alan S., Brent P. Little, Christoph Rahner, Darkhan Utepbergenov, Zenta Walther, and James M. Anderson. 2007. “The Unique-5 and -6 Motifs of ZO-1 Regulate Tight Junction Strand Localization and Scaffolding Properties.” *Molecular Biology of the Cell* 18 (3): 721–31.

Fanning, Alan S., Thomas Y. Ma, and James Melvin Anderson. 2002. “Isolation and Functional Characterization of the Actin Binding Region in the Tight Junction Protein ZO-1.” *FASEB Journal: Official Publication of the Federation of American Societies for Experimental Biology* 16 (13): 1835–37.

Fanning, A. S., B. J. Jameson, L. A. Jesaitis, and J. M. Anderson. 1998. “The Tight Junction Protein ZO-1 Establishes a Link between the Transmembrane Protein Occludin and the Actin Cytoskeleton.” *The Journal of Biological Chemistry* 273 (45): 29745–53.

Franke, W. W. 2009. “Discovering the Molecular Components of Intercellular Junctions—a Historical View.” *Cold Spring Harbor Perspectives in Biology*. http://cshperspectives.cshlp.org/content/1/3/a003061.short.

Gagnon, James A., Eivind Valen, Summer B. Thyme, Peng Huang, Laila Akhmetova, Andrea Pauli, Tessa G. Montague, Steven Zimmerman, Constance Richter, and Alexander F. Schier. 2014. “Efficient Mutagenesis by Cas9 Protein-Mediated Oligonucleotide Insertion and Large-Scale Assessment of Single-Guide RNAs.” *PloS One* 9 (5): e98186.

Godsel, L. M., S. Getsios, A. C. Huen, and K. J. Green. 2004. “The Molecular Composition and Function of Desmosomes.” *Handbook of Experimental Pharmacology*, no. 165: 137–93.

Goehring, Nathan W., and Stephan W. Grill. 2013. “Cell Polarity: Mechanochemical Patterning.” *Trends in Cell Biology* 23 (2): 72–80.

Gomez, Guillermo A., Robert W. McLachlan, and Alpha S. Yap. 2011. “Productive Tension: Force-Sensing and Homeostasis of Cell–cell Junctions.” *Trends in Cell Biology* 21 (9): 499–505.

Guillemot, Laurent, Diego Guerrera, Domenica Spadaro, Rocio Tapia, Lionel Jond, and Sandra Citi. 2014. “MgcRacGAP Interacts with Cingulin and Paracingulin to Regulate Rac1 Activation and Development of the Tight Junction Barrier during Epithelial Junction Assembly.” *Molecular Biology of the Cell* 25 (13): 1995–2005.

Hannezo, Edouard, and Carl-Philipp Heisenberg. 2019. “Mechanochemical Feedback Loops in Development and Disease.” *Cell* 178 (1): 12–25.

Hashimoto, Yutaka, Noriyuki Kinoshita, Todd M. Greco, Joel D. Federspiel, Pierre M. Jean Beltran, Naoto Ueno, and Ileana M. Cristea. 2019. “Mechanical Force Induces Phosphorylation-Mediated Signaling That Underlies Tissue Response and Robustness in Xenopus Embryos.” *Cell Systems* 8 (3): 226–41.e7.

Hatte, Guillaume, Claude Prigent, and Jean-Pierre Tassan. 2018. “Tight Junctions Negatively Regulate Mechanical Forces Applied to Adherens Junctions in Vertebrate Epithelial Tissue.” *Journal of Cell Science* 131 (3). https://doi.org/10.1242/jcs.208736.

Holloway, Beth A., Sol Gomez de la Torre Canny, Ying Ye, Diane C. Slusarski, Christina M. Freisinger, Roland Dosch, Margaret M. Chou, Daniel S. Wagner, and Mary C. Mullins. 2009. “A Novel Role for MAPKAPK2 in Morphogenesis during Zebrafish Development.” *PLoS Genetics* 5 (3): e1000413.

Hyman, Anthony A., Christoph A. Weber, and Frank Jülicher. 2014. “Liquid-Liquid Phase Separation in Biology.” *Annual Review of Cell and Developmental Biology* 30: 39–58.

Iioka, Hidekazu, Naoto Ueno, and Noriyuki Kinoshita. 2004. “Essential Role of MARCKS in Cortical Actin Dynamics during Gastrulation Movements.” *The Journal of Cell Biology* 164 (2): 169–74.

Itoh, Masahiko, Sachiko Tsukita, Yuji Yamazaki, and Hiroyuki Sugimoto. 2012. “Rho GTP Exchange Factor ARHGEF11 Regulates the Integrity of Epithelial Junctions by Connecting ZO-1 and RhoA-Myosin II Signaling.” *Proceedings of the National Academy of Sciences of the United States of America* 109 (25): 9905–10.

Jayashankar, V., M. J. Nguyen, B. W. Carr, and D. C. Zheng. 2013. “Protein Phosphatase 1 β Paralogs Encode the Zebrafish Myosin Phosphatase Catalytic Subunit.” *PloS One*. https://journals.plos.org/plosone/article?id=10.1371/journal.pone.0075766.

Johnson, Jodi L., Nicole A. Najor, and Kathleen J. Green. 2014. “Desmosomes: Regulators of Cellular Signaling and Adhesion in Epidermal Health and Disease.” *Cold Spring Harbor Perspectives in Medicine* 4 (11): a015297.

Kato, Masato, Tina W. Han, Shanhai Xie, Kevin Shi, Xinlin Du, Leeju C. Wu, Hamid Mirzaei, et al. 2012. “Cell-Free Formation of RNA Granules: Low Complexity Sequence Domains Form Dynamic Fibers within Hydrogels.” *Cell* 149 (4): 753–67.

Keller, Philipp J., Annette D. Schmidt, Joachim Wittbrodt, and Ernst H. K. Stelzer. 2008. "Reconstruction of Zebrafish Early Embryonic Development by Scanned Light Sheet Microscopy." *Science* 322 (5904): 1065–69.

Kimmel, C. B., W. W. Ballard, S. R. Kimmel, B. Ullmann, and T. F. Schilling. 1995. "Stages of Embryonic Development of the Zebrafish." *Developmental Dynamics: An Official Publication of the American Association of Anatomists* 203 (3): 253–310.

Kimmel, Robin A., and Dirk Meyer. 2010. "Molecular Regulation of Pancreas Development in Zebrafish." *Methods in Cell Biology* 100: 261–80.

Köppen, Mathias, Beatriz García Fernández, Lara Carvalho, Antonio Jacinto, and Carl-Philipp Heisenberg. 2006. "Coordinated Cell-Shape Changes Control Epithelial Movement in Zebrafish and Drosophila." *Development* 133 (14): 2671–81.

Kwan, K. M., E. Fujimoto, and C. Grabher. 2007. "The Tol2kit: A Multisite Gateway- based Construction Kit for Tol2 Transposon Transgenesis Constructs." *Dynamics: An Official ….* https://onlinelibrary.wiley.com/doi/abs/10.1002/dvdy.21343.

Labun, Kornel, Tessa G. Montague, James A. Gagnon, Summer B. Thyme, and Eivind Valen. 2016. "CHOPCHOP v2: A Web Tool for the next Generation of CRISPR Genome Engineering." *Nucleic Acids Research* 44 (W1): W272–76.

Ladoux, Benoit, Ester Anon, Mireille Lambert, Aleksandr Rabodzey, Pascal Hersen, Axel Buguin, Pascal Silberzan, and René-Marc Mège. 2010. "Strength Dependence of Cadherin-Mediated Adhesions." *Biophysical Journal* 98 (4): 534–42.

Lecuit, Thomas, Pierre-François Lenne, and Edwin Munro. 2011. "Force Generation, Transmission, and Integration during Cell and Tissue Morphogenesis." *Annual Review of Cell and Developmental Biology* 27 (July): 157–84.

Lepage, Stephanie E., and Ashley E. E. Bruce. 2010. "Zebrafish Epiboly: Mechanics and Mechanisms." *The International Journal of Developmental Biology* 54 (8-9): 1213–28.

Li, Pilong, Sudeep Banjade, Hui-Chun Cheng, Soyeon Kim, Baoyu Chen, Liang Guo, Marc Llaguno, et al. 2012. "Phase Transitions in the Assembly of Multivalent Signalling Proteins." *Nature* 483 (7389): 336–40.

Li, Qi, Anthony Lau, Terence J. Morris, Lin Guo, Christopher B. Fordyce, and Elise F. Stanley. 2004. "A Syntaxin 1, Gαo, and N-Type Calcium Channel Complex at a Presynaptic Nerve Terminal: Analysis by Quantitative Immunocolocalization." *The Journal of Neuroscience: The Official Journal of the Society for Neuroscience* 24 (16): 4070–81.

Lye, Ming F., Alan S. Fanning, Ying Su, James M. Anderson, and Arnon Lavie. 2010. "Insights into Regulated Ligand Binding Sites from the Structure of ZO-1 Src Homology 3-Guanylate Kinase Module." *The Journal of Biological Chemistry* 285 (18): 13907–17.

Maître, Jean-Léon, Hélène Berthoumieux, Simon Frederik Gabriel Krens, Guillaume Salbreux, Frank Jülicher, Ewa Paluch, and Carl-Philipp Heisenberg. 2012. "Adhesion Functions in Cell Sorting by Mechanically Coupling the Cortices of Adhering Cells." *Science* 338 (6104): 253–56.

Matter, Karl, and Maria S. Balda. 2003. "Signalling to and from Tight Junctions." *Nature Reviews. Molecular Cell Biology* 4 (3): 225–36.

Mayer, Mirjam, Martin Depken, Justin S. Bois, Frank Jülicher, and Stephan W. Grill. 2010. "Anisotropies in Cortical Tension Reveal the Physical Basis of Polarizing Cortical Flows." *Nature* 467 (7315): 617–21.

Meeker, Nathan D., Sarah A. Hutchinson, Linh Ho, and Nikolaus S. Trede. 2007. "Method for Isolation of PCR-Ready Genomic DNA from Zebrafish Tissues." *BioTechniques* 43 (5): 610, 612, 614.

Miesfeld, Joel B., Gaia Gestri, Brian S. Clark, Michael A. Flinn, Richard J. Poole, Jason R. Bader, Joseph C. Besharse, Stephen W. Wilson, and Brian A. Link. 2015. "Yap and Taz Regulate Retinal Pigment Epithelial Cell Fate." *Development* 142 (17): 3021–32.

Monahan, Zachary, Veronica H. Ryan, Abigail M. Janke, Kathleen A. Burke, Shannon N. Rhoads, Gül H. Zerze, Robert O'Meally, et al. 2017. "Phosphorylation of the FUS Low-Complexity Domain Disrupts Phase Separation, Aggregation, and Toxicity." *The EMBO Journal* 36 (20): 2951–67.

Montague, Tessa G., José M. Cruz, James A. Gagnon, George M. Church, and Eivind Valen. 2014. "CHOPCHOP: A CRISPR/Cas9 and TALEN Web Tool for Genome Editing." *Nucleic Acids Research* 42 (Web Server issue): W401–7.

Montero, Juan-Antonio, Lara Carvalho, Michaela Wilsch-Bräuninger, Beate Kilian, Chigdem Mustafa, and Carl-Philipp Heisenberg. 2005. "Shield Formation at the Onset of Zebrafish Gastrulation." *Development* 132 (6): 1187–98.

Munro, Edwin, Jeremy Nance, and James R. Priess. 2004. "Cortical Flows Powered by Asymmetrical Contraction Transport PAR Proteins to Establish and Maintain Anterior-Posterior Polarity in the Early C. Elegans Embryo." *Developmental Cell* 7 (3): 413–24.

Nekrasova, Oxana, and Kathleen J. Green. 2013. “Desmosome Assembly and Dynamics.” *Trends in Cell Biology* 23 (11): 537–46.
Niessen, Carien M. 2007. “Tight Junctions/adherens Junctions: Basic Structure and Function.” *The Journal of Investigative Dermatology* 127 (11): 2525–32.
Otani, Tetsuhisa, Tetsuo Ichii, Shinya Aono, and Masatoshi Takeichi. 2006. “Cdc42 GEF Tuba Regulates the Junctional Configuration of Simple Epithelial Cells.” *The Journal of Cell Biology* 175 (1): 135–46.
Preibisch, Stephan, Stephan Saalfeld, and Pavel Tomancak. 2009. “Globally Optimal Stitching of Tiled 3D Microscopic Image Acquisitions.” *Bioinformatics* 25 (11): 1463–65.
Schindelin, Johannes, Ignacio Arganda-Carreras, Erwin Frise, Verena Kaynig, Mark Longair, Tobias Pietzsch, Stephan Preibisch, et al. 2012. “Fiji: An Open-Source Platform for Biological-Image Analysis.” *Nature Methods* 9 (7): 676–82.
Shaner, Nathan C., Gerard G. Lambert, Andrew Chammas, Yuhui Ni, Paula J. Cranfill, Michelle A. Baird, Brittney R. Sell, et al. 2013. “A Bright Monomeric Green Fluorescent Protein Derived from Branchiostoma Lanceolatum.” *Nature Methods* 10 (5): 407–9.
Shen, Le, Christopher R. Weber, and Jerrold R. Turner. 2008. “The Tight Junction Protein Complex Undergoes Rapid and Continuous Molecular Remodeling at Steady State.” *The Journal of Cell Biology* 181 (4): 683–95.
Shin, Kunyoo, Vanessa C. Fogg, and Ben Margolis. 2006. “Tight Junctions and Cell Polarity.” *Annual Review of Cell and Developmental Biology* 22: 207–35.
Smutny, Michael, Zsuzsa Ákos, Silvia Grigolon, Shayan Shamipour, Verena Ruprecht, Daniel Čapek, Martin Behrndt, et al. 2017. “Friction Forces Position the Neural Anlage.” *Nature Cell Biology* 19 (4): 306–17.
Sommer, C., C. Straehle, U. Köthe, and F. A. Hamprecht. 2011. “Ilastik: Interactive Learning and Segmentation Toolkit.” In *2011 IEEE International Symposium on Biomedical Imaging: From Nano to Macro*, 230–33.
Spadaro, Domenica, Shimin Le, Thierry Laroche, Isabelle Mean, Lionel Jond, Jie Yan, and Sandra Citi. 2017. “Tension-Dependent Stretching Activates ZO-1 to Control the Junctional Localization of Its Interactors.” *Current Biology: CB* 27 (24): 3783–95.e8.
Style, Robert W., Tianqi Sai, Nicoló Fanelli, Mahdiye Ijavi, Katrina Smith-Mannschott, Qin Xu, Lawrence A. Wilen, and Eric R. Dufresne. 2018. “Liquid-Liquid Phase Separation in an Elastic Network.” *Physical Review X* 8 (1): 011028.
Takesono, Aya, Julian Moger, Sumera Farooq, Emma Cartwright, Igor B. Dawid, Stephen W. Wilson, and Tetsuhiro Kudoh. 2012. “Solute Carrier Family 3 Member 2 (Slc3a2) Controls Yolk Syncytial Layer (YSL) Formation by Regulating Microtubule Networks in the Zebrafish Embryo.” *Proceedings of the National Academy of Sciences of the United States of America* 109 (9): 3371–76.
Talbot, Jared Coffin, and Sharon L. Amacher. 2014. “A Streamlined CRISPR Pipeline to Reliably Generate Zebrafish Frameshifting Alleles.” *Zebrafish* 11 (6): 583–85.
Thielicke, William, and Eize J. Stamhuis. 2014. “PIVlab – Towards User-Friendly, Affordable and Accurate Digital Particle Image Velocimetry in MATLAB.” *Journal of Open Research Software*. https://doi.org/10.5334/jors.bl.
Tornavaca, O., M. Chia, N. Dufton, and L. O. Almagro. 2015. “ZO-1 Controls Endothelial Adherens Junctions, Cell–cell Tension, Angiogenesis, and Barrier Formation.” *The Journal of Cell Biology*. http://jcb.rupress.org/content/208/6/821.short.
Utepbergenov, Darkhan I., Alan S. Fanning, and James M. Anderson. 2006. “Dimerization of the Scaffolding Protein ZO-1 through the Second PDZ Domain.” *The Journal of Biological Chemistry* 281 (34): 24671–77.
Van Itallie, Christina M., and James M. Anderson. 2014. “Architecture of Tight Junctions and Principles of Molecular Composition.” *Seminars in Cell & Developmental Biology* 36 (December): 157–65.
Villefranc, Jacques A., Julio Amigo, and Nathan D. Lawson. 2007. “Gateway Compatible Vectors for Analysis of Gene Function in the Zebrafish.” *Developmental Dynamics: An Official Publication of the American Association of Anatomists* 236 (11): 3077–87.
Watabe-Uchida, M., N. Uchida, Y. Imamura, A. Nagafuchi, K. Fujimoto, T. Uemura, S. Vermeulen, F. van Roy, E. D. Adamson, and M. Takeichi. 1998. “Alpha-Catenin-Vinculin Interaction Functions to Organize the Apical Junctional Complex in Epithelial Cells.” *The Journal of Cell Biology* 142 (3): 847–57.
Weiss, E. E., M. Kroemker, A. H. Rüdiger, B. M. Jockusch, and M. Rüdiger. 1998. “Vinculin Is Part of the Cadherin-Catenin Junctional Complex: Complex Formation between Alpha-Catenin and

Vinculin." *The Journal of Cell Biology* 141 (3): 755–64.
Westerfield, Monte. 2007. *The Zebrafish Book: A Guide for the Laboratory Use of Zebrafish (Danio Rerio)*. University of Oregon press.
Wheelock, Margaret J., and Keith R. Johnson. 2003. "Cadherin-Mediated Cellular Signaling." *Current Opinion in Cell Biology* 15 (5): 509–14.
Wittchen, Erika S., Julie Haskins, and Bruce R. Stevenson. 2003. "NZO-3 Expression Causes Global Changes to Actin Cytoskeleton in Madin-Darby Canine Kidney Cells: Linking a Tight Junction Protein to Rho GTPases." *Molecular Biology of the Cell* 14 (5): 1757–68.
Ye, Fei, Menglong Zeng, and Mingjie Zhang. 2018. "Mechanisms of MAGUK-Mediated Cellular Junctional Complex Organization." *Current Opinion in Structural Biology* 48 (February): 6–15.
Yonemura, Shigenobu, Yuko Wada, Toshiyuki Watanabe, Akira Nagafuchi, and Mai Shibata. 2010. "Alpha-Catenin as a Tension Transducer That Induces Adherens Junction Development." *Nature Cell Biology* 12 (6): 533–42.
Yu, Dan, Amanda M. Marchiando, Christopher R. Weber, David R. Raleigh, Yingmin Wang, Le Shen, and Jerrold R. Turner. 2010. "MLCK-Dependent Exchange and Actin Binding Region-Dependent Anchoring of ZO-1 Regulate Tight Junction Barrier Function." *Proceedings of the National Academy of Sciences of the United States of America* 107 (18): 8237–41.
Zeng, Menglong, Yuan Shang, Yoichi Araki, Tingfeng Guo, Richard L. Huganir, and Mingjie Zhang. 2016. "Phase Transition in Postsynaptic Densities Underlies Formation of Synaptic Complexes and Synaptic Plasticity." *Cell* 166 (5): 1163–75.e12.
Zihni, Ceniz, Clare Mills, Karl Matter, and Maria S. Balda. 2016. "Tight Junctions: From Simple Barriers to Multifunctional Molecular Gates." *Nature Reviews. Molecular Cell Biology* 17 (9): 564–80.
Zihni, Ceniz, and Stephen James Terry. 2015. "RhoGTPase Signalling at Epithelial Tight Junctions: Bridging the GAP between Polarity and Cancer." *The International Journal of Biochemistry & Cell Biology* 64 (July): 120–25.

KEY RESOURCES TABLE

REAGENT or RESOURCE	SOURCE	IDENTIFIER
Antibodies		
Anti-ZO-1 mouse Monoclonal Antibody (ZO1-1A12)	Thermo Fisher Scientific	Cat# 33-9100, RRID:AB_2533147
Anti-ZO-3 rabbit Antibody	Benais-Pont et al. 2003	N/A
Anti-E-Cadherin (zebrafish) rabbit Antibody	Maître et al. 2012	N/A
Anti-alpha-Catenin antibody produced in rabbit	Sigma-Aldrich	Cat# C2081, RRID:AB_476830
Monoclonal Anti-beta-Catenin antibody produced in mouse	Sigma-Aldrich	Cat# C7207, RRID:AB_476865
Alexa Fluor 488 goat anti-mouse IgG (H+L)	Thermo Fisher Scientific	Cat# A-11001; RRID:AB_2534069
Alexa Fluor 488 goat anti-rabbit IgG (H+L)	Thermo Fisher Scientific	Cat# A-11008; RRID: AB_143165
Alexa Fluor 594 Goat Anti-Mouse IgG (H+L)	Thermo Fisher Scientific	Cat# A-11005, RRID:AB_2534073
Alexa Fluor 546 goat anti-rabbit IgG (H+L)	Thermo Fisher Scientific	Cat# A-11010, RRID:AB_2534077
Alexa Fluor 647 goat anti-mouse IgG (H+L)	Thermo Fisher Scientific	Cat# A-21235, RRID:AB_2535804
Alexa Fluor 647 goat anti-rabbit IgG (H+L)	Thermo Fisher Scientific	Cat# A-21244, RRID:AB_2535812
Bacterial and Virus Strains		
Biological Samples		
Chemicals, Peptides, and Recombinant Proteins		
GFP protein	Gift from Alf Honigmann (MPI CBG Dresden)	N/A
Latrunculin B	EMD Millipore	Cat# 428020-1MG
DMSO	Sigma	Cat# D8418-100ML; CAS: 67-68-5
Critical Commercial Assays		
Deposited Data		
Experimental Models: Cell Lines		
Experimental Models: Organisms/Strains		
Zebrafish: TL wild-type		N/A
Zebrafish: AB wild-type		N/A
Zebrafish: Tuebingen wild-type		N/A
Zebrafish: MZ*zo-1b*	this study	N/A
Zebrafish: MZ*zo-3*	this study	N/A
Zebrafish: MZ*zo-1b/3*	this study	N/A
Zebrafish: Tg(*actb2:mNeonGreen-zo-1b*)	this study	N/A
Zebrafish: MZ*zo-1b/3*; Tg(*actb2:mNeonGreen-zo-1b*)	this study	N/A
Zebrafish: MZ*zo-1b/3*; Tg(*actb2:mNeonGreen-zo-1bΔABR*)	this study	N/A
Zebrafish: Tg(*actb1:Utr-mCherry*)	Behrndt et al. 2012	N/A

Zebrafish: Tg(*actb1:myl12.1-GFP*)	Behrndt et al. 2012; Maître et al. 2012	RRID: ZFIN_ ZDB-TGCONSTRCT-130108-2
Zebrafish: Tg(*actb1:myl12.1-mcherry*)	Behrndt et al. 2012; Maître et al. 2012	N/A
Zebrafish: Tg(*actb1:myl12.1-mcherry; actb2:mNeonGreen-zo-1b*)	this study	N/A
Zebrafish: Tg(*actb2:mNeonGreen-zo-1b; actb1:Utrophin-mcherry*)	this study	N/A
Tg(*actb2:Lyn-TdTomato*)	Compagnon et al. 2014	ZFIN ID: ZDB-TGCONSTRCT-130516-1
Oligonucleotides		
Recombinant DNA		
pCS2-*GFP-zo-1b* (zebrafish version)	This study	N/A
pCS2-*mcherry-zo-1b* (zebrafish version)	This study	N/A
pCS2-*GFP-zo-3* (zebrafish version)	This study	N/A
pCS2-*GFP-zo-3_4mismatch* (zebrafish version)	This study	N/A
pCS2-*mcherry-zo-3* (zebrafish version)	This study	N/A
pCS2-*mcherry-cingulin-like 1* (zebrafish version)	This study	N/A
pCS2-*Occludin-A-mNEONgreen* (zebrafish version)	This study	N/A
pCS2-*GFP-Claudin D* (zebrafish version)	Gift from Ashley Bruce (University of Toronto)	N/A
pCS2-*GFP-zo-1b-ΔC* (zebrafish version)	This study	N/A
pCS2-*GFP-zo-1b-ΔABR* (zebrafish version)	This study	N/A
pTol2-*actb2:mNEONgreen-zo-1b* (zebrafish version)	This study	N/A
pTol2-*actb2:mNeonGreen-zo-1bΔABR* (zebrafish version)	This study	N/A
pCS2-*membrane-RFP*	Iioka, Ueno, and Kinoshita 2004	N/A
pCS2-*membrane-GFP*	R. A. Kimmel and Meyer 2010	N/A
pCS2-*lifeact-RFP*	Behrndt et al. 2012	N/A
pCS2-*H2A-mCherry*	Arboleda-Estudillo et al. 2010	N/A
pCS2-*H2B-GFP*	Keller et al. 2008	N/A
Software and Algorithms		
Fiji	Schindelin et al. 2012	https://fiji.sc/
Imaris	Bitplane	http://www.bitplane.com/imaris
Excel	Microsoft	https://products.office.com/
GraphPad Prism	GraphPad Software	https://www.graphpad.com/scientific-software/prism/
PIVlab	Thielicke and Stamhuis 2014	https://pivlab.blogspot.com/
MATLAB	MATLAB Software	https://www.mathworks.com/products/matlab.html

Ilastik	Sommer et al. 2011	https://www.ilastik.org/
R	The R Project for Statistical Computing	https://www.r-project.org
Other		

Figure 1

Click here to access/download;Figure;Figure1_V5.pdf

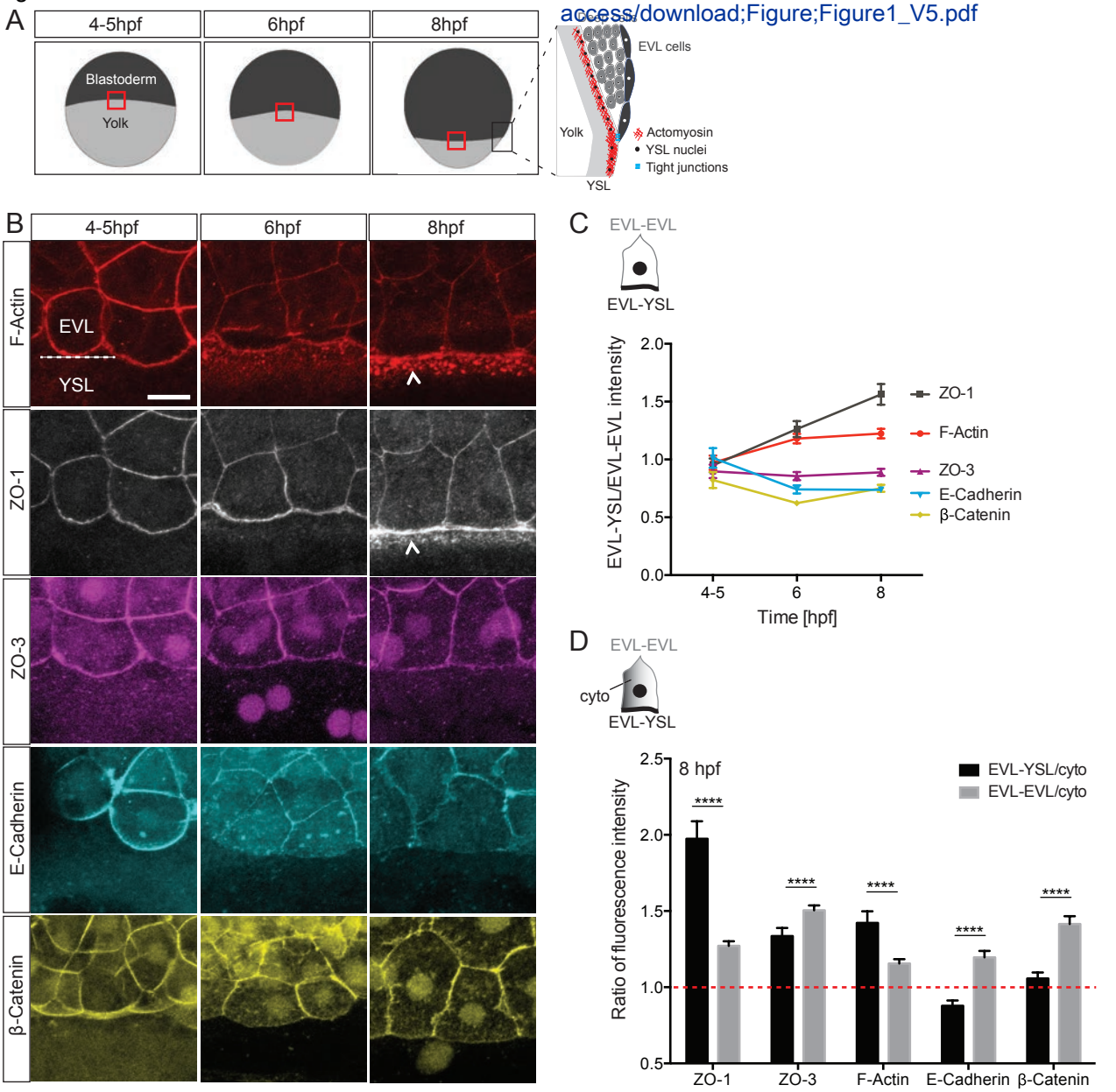

Figure 2

Click here to access/download;Figure;Figure2_V10.pdf

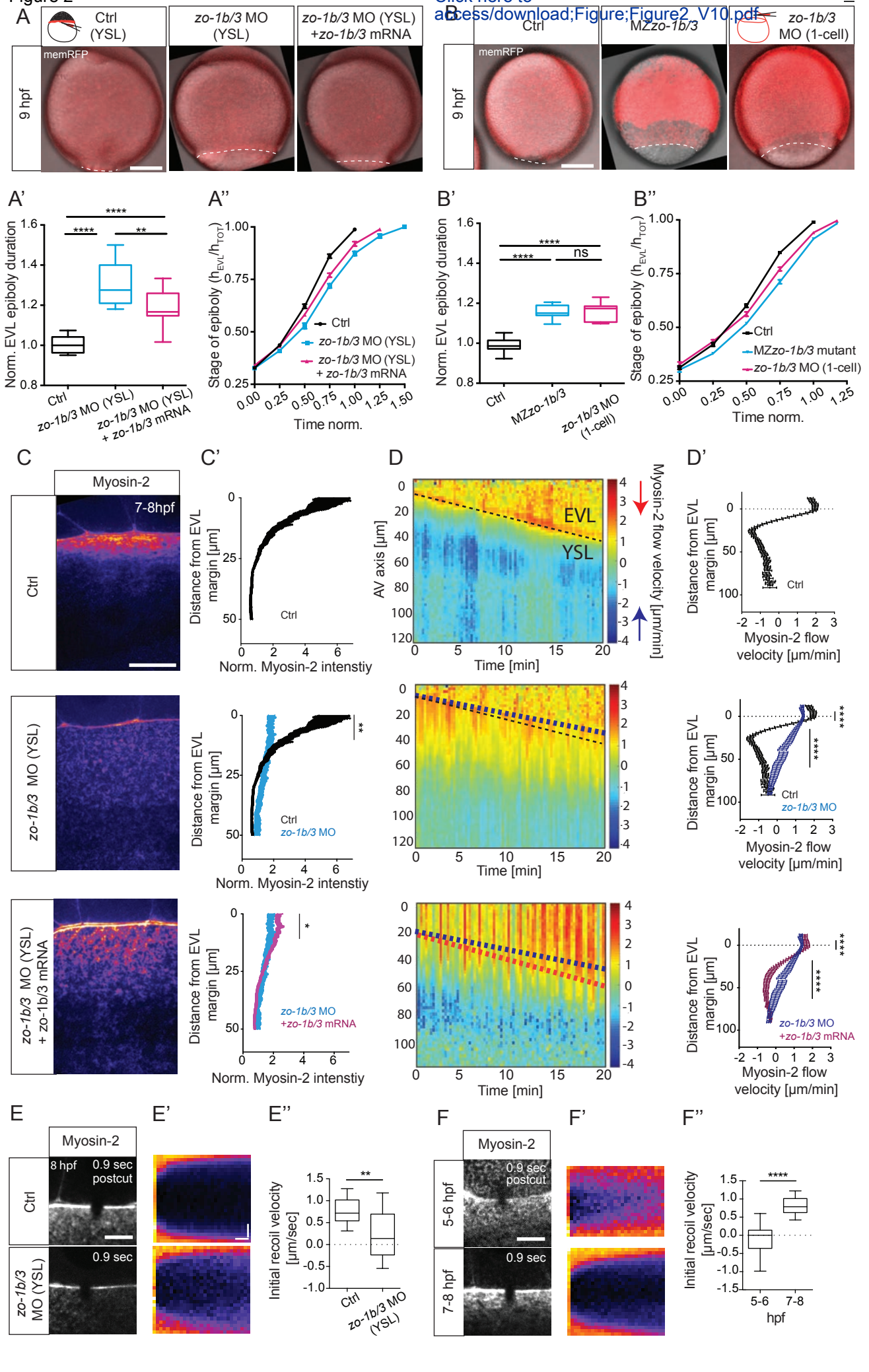

Figure 3

Click here to access/download;Figure;Figure3_V5.pdf

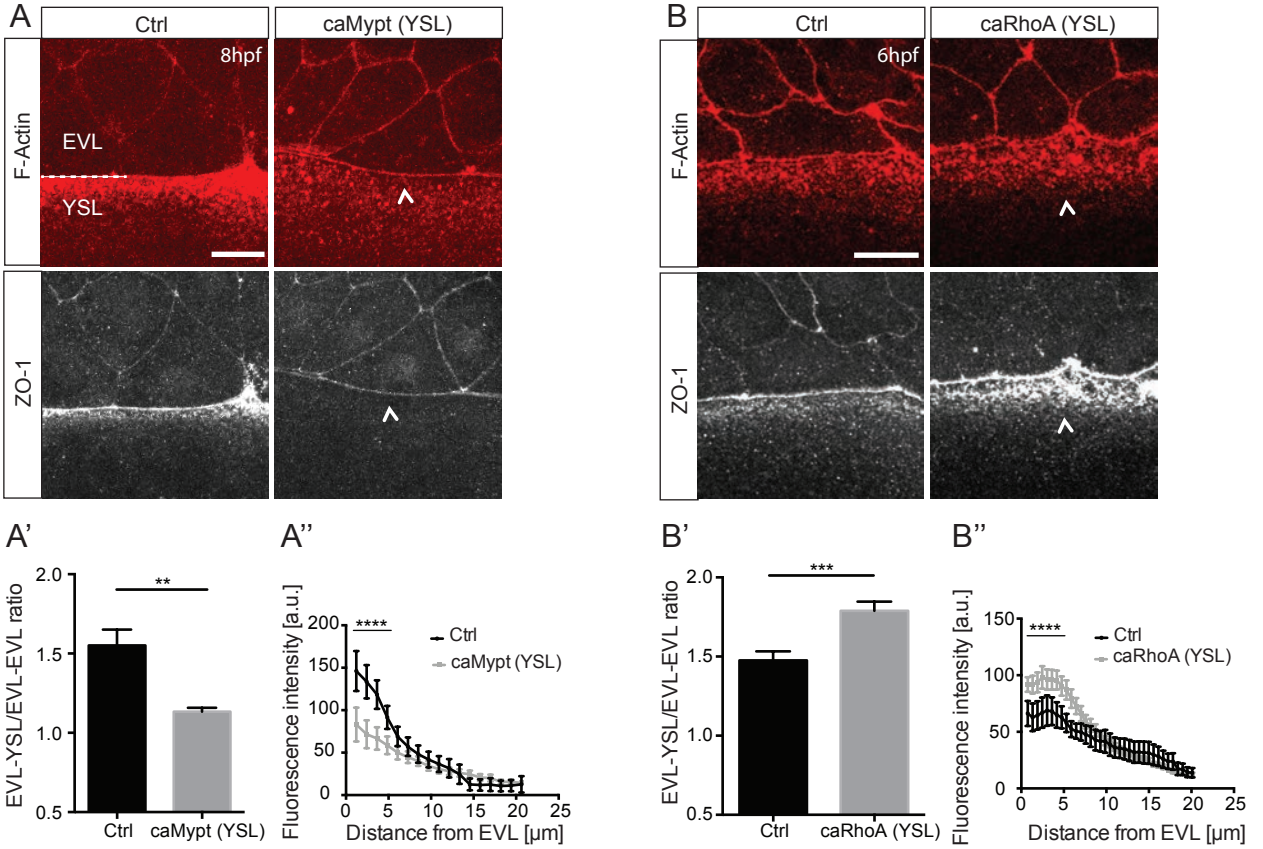

Figure 4

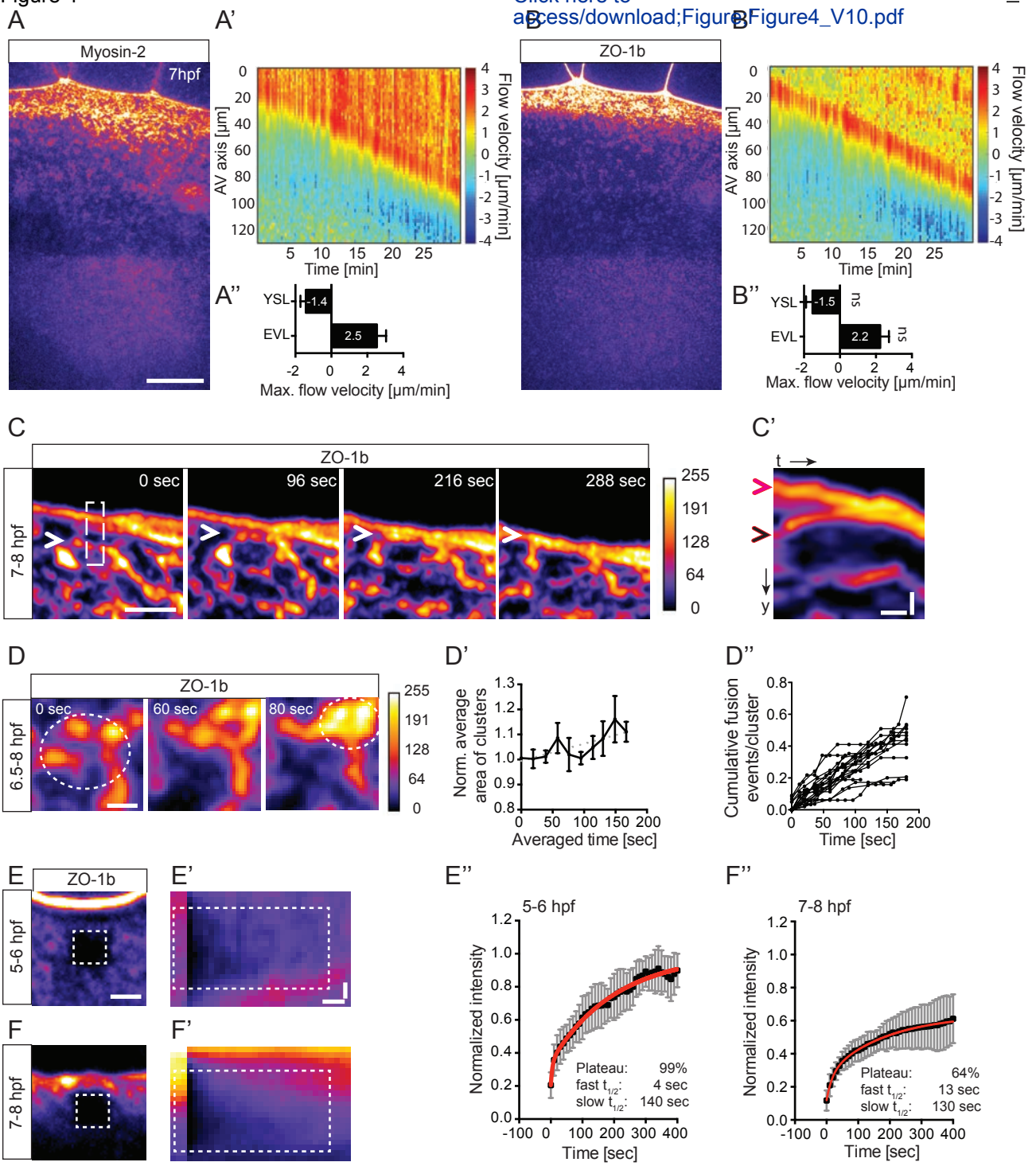

Figure 5

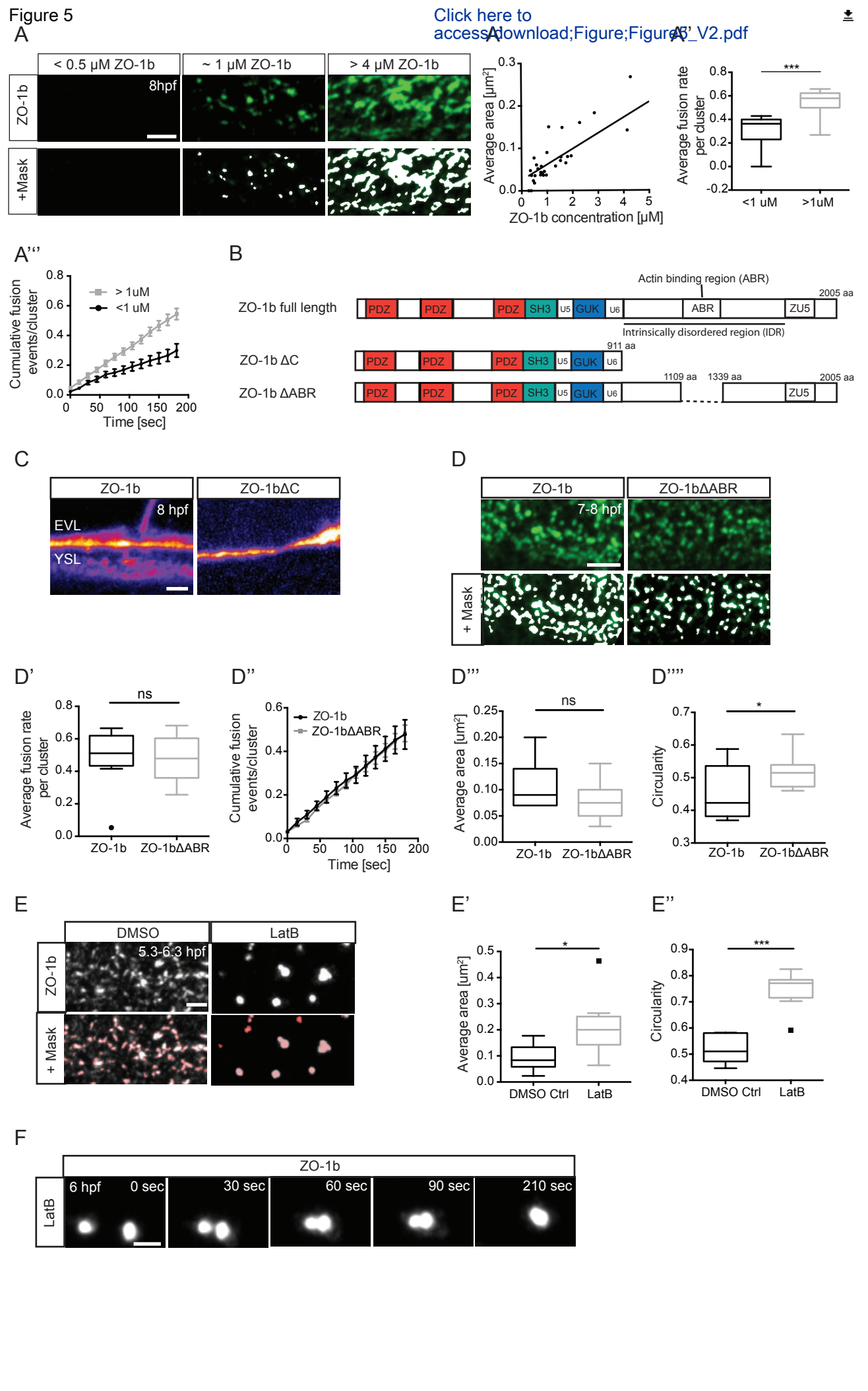

Figure 6

Click here to access/download;Figure;Figure6_V1.pdf

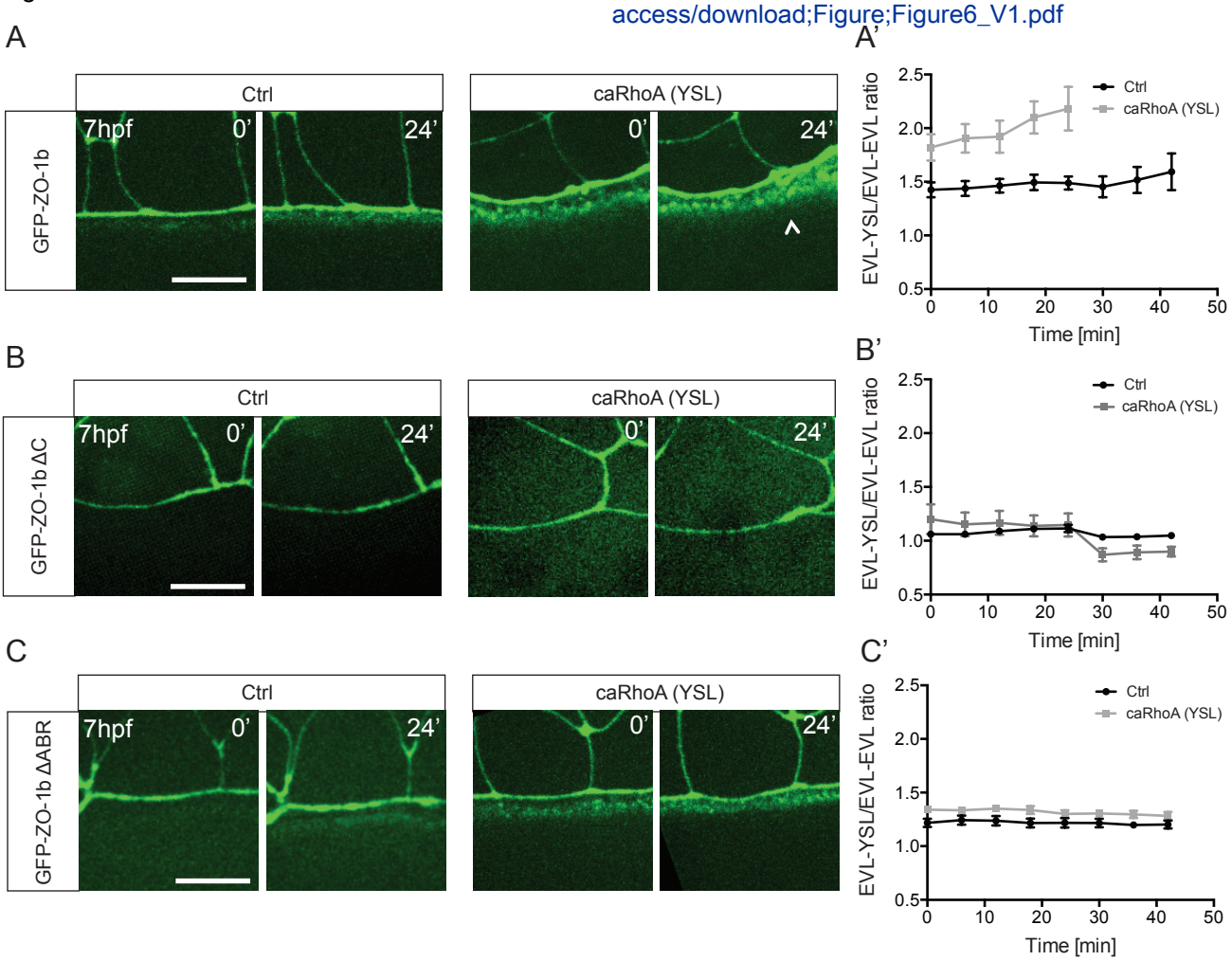

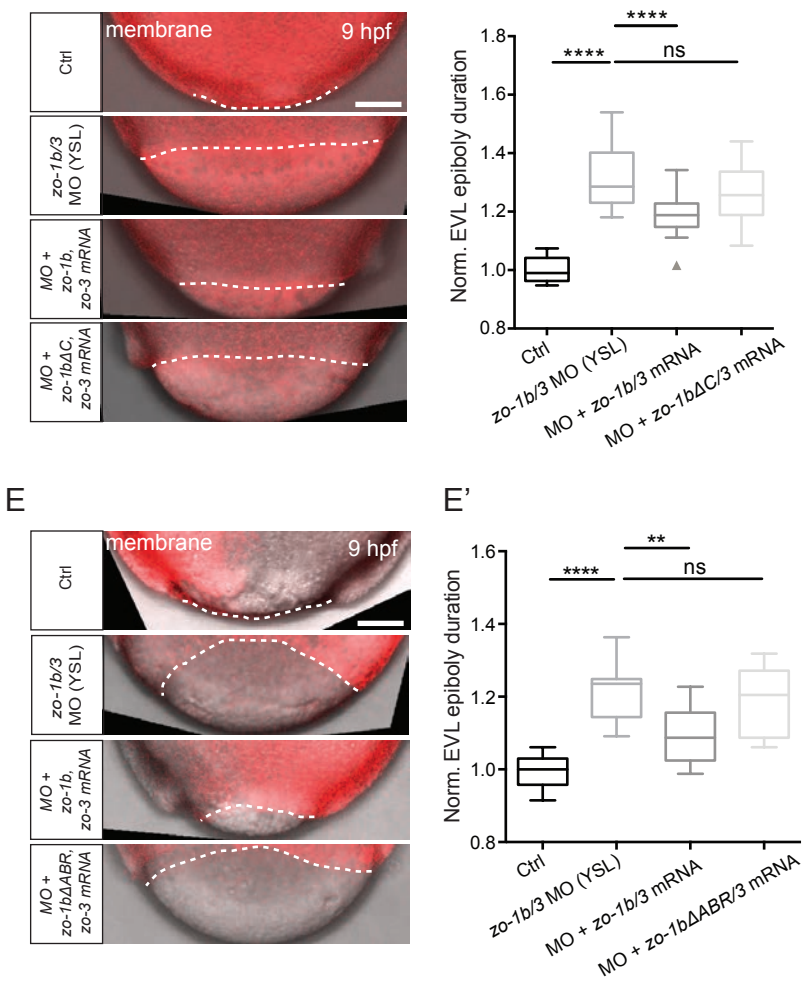

Supplemental Figure 1

Click here to access/download;Supplemental Figure;FigureS1_V5.pdf

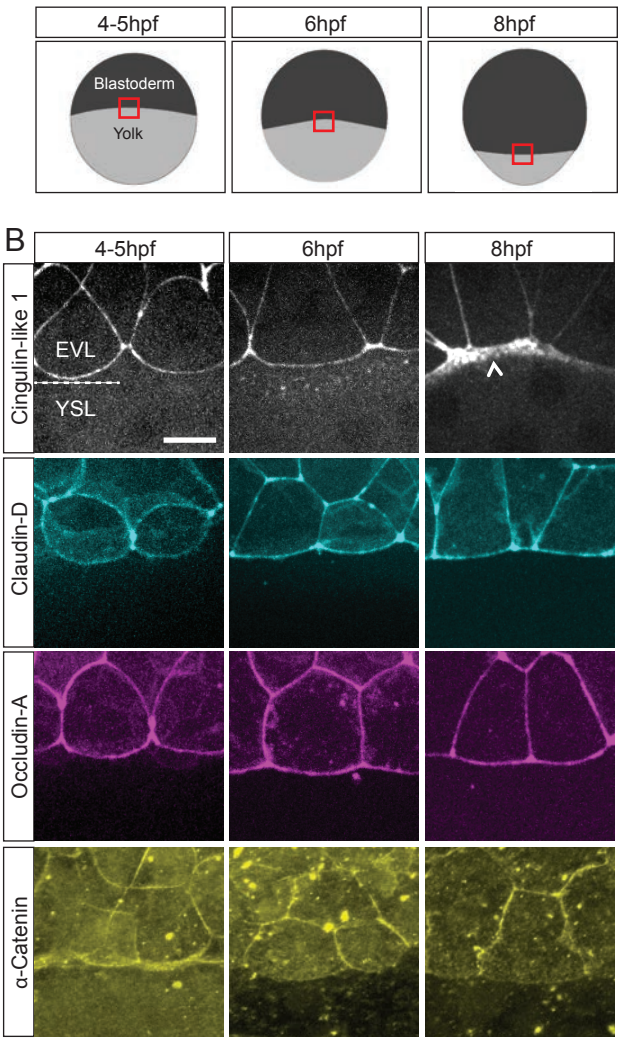

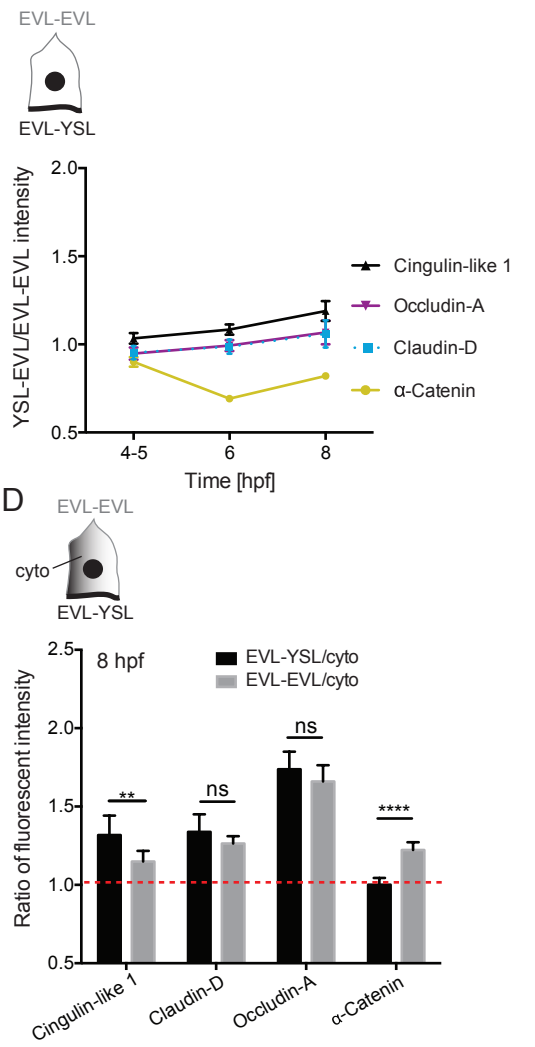

Supplemental Figure 2

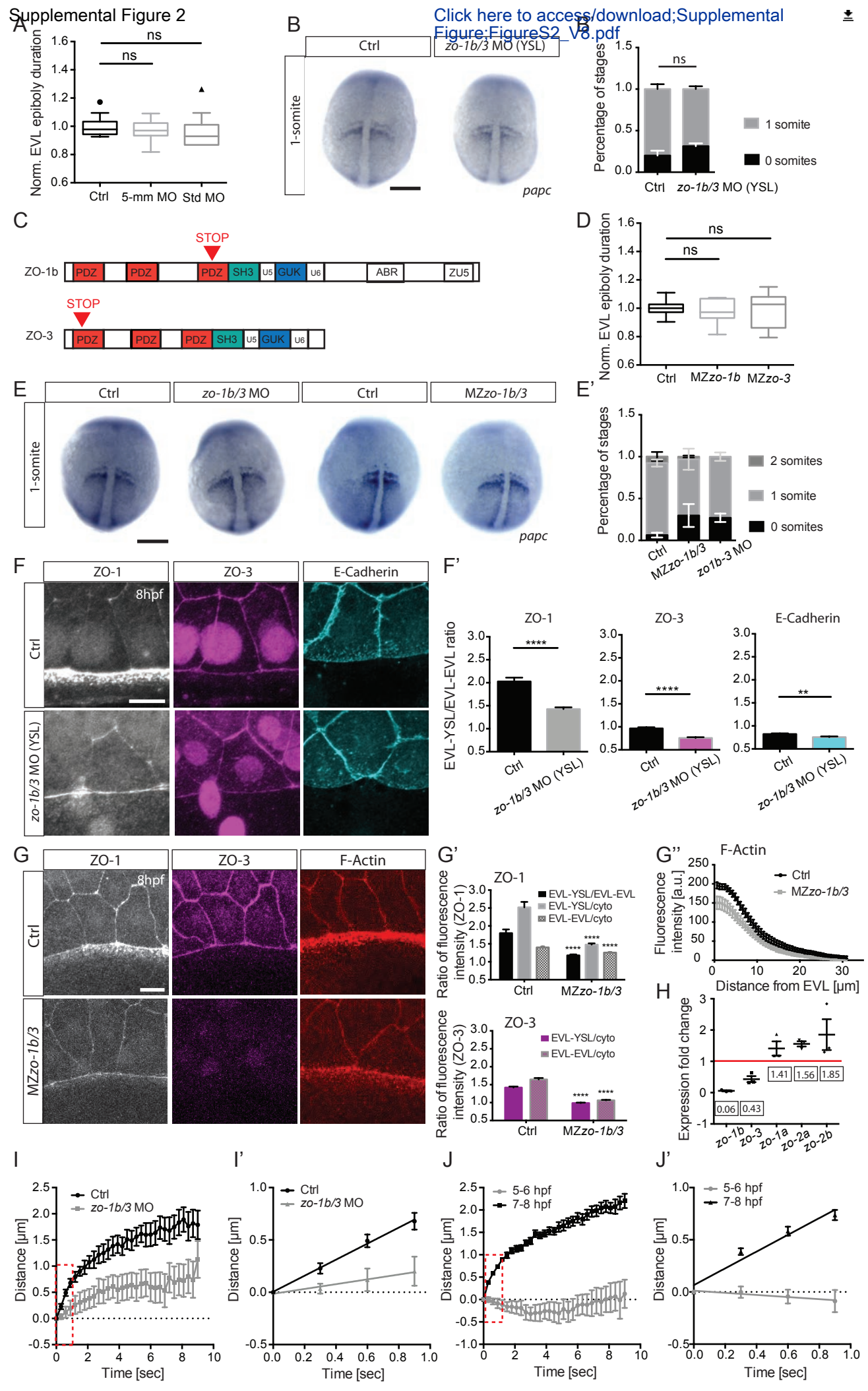

Supplemental Figure 3

Click here to access/download;Supplemental Figure;FigureS3_V5.pdf

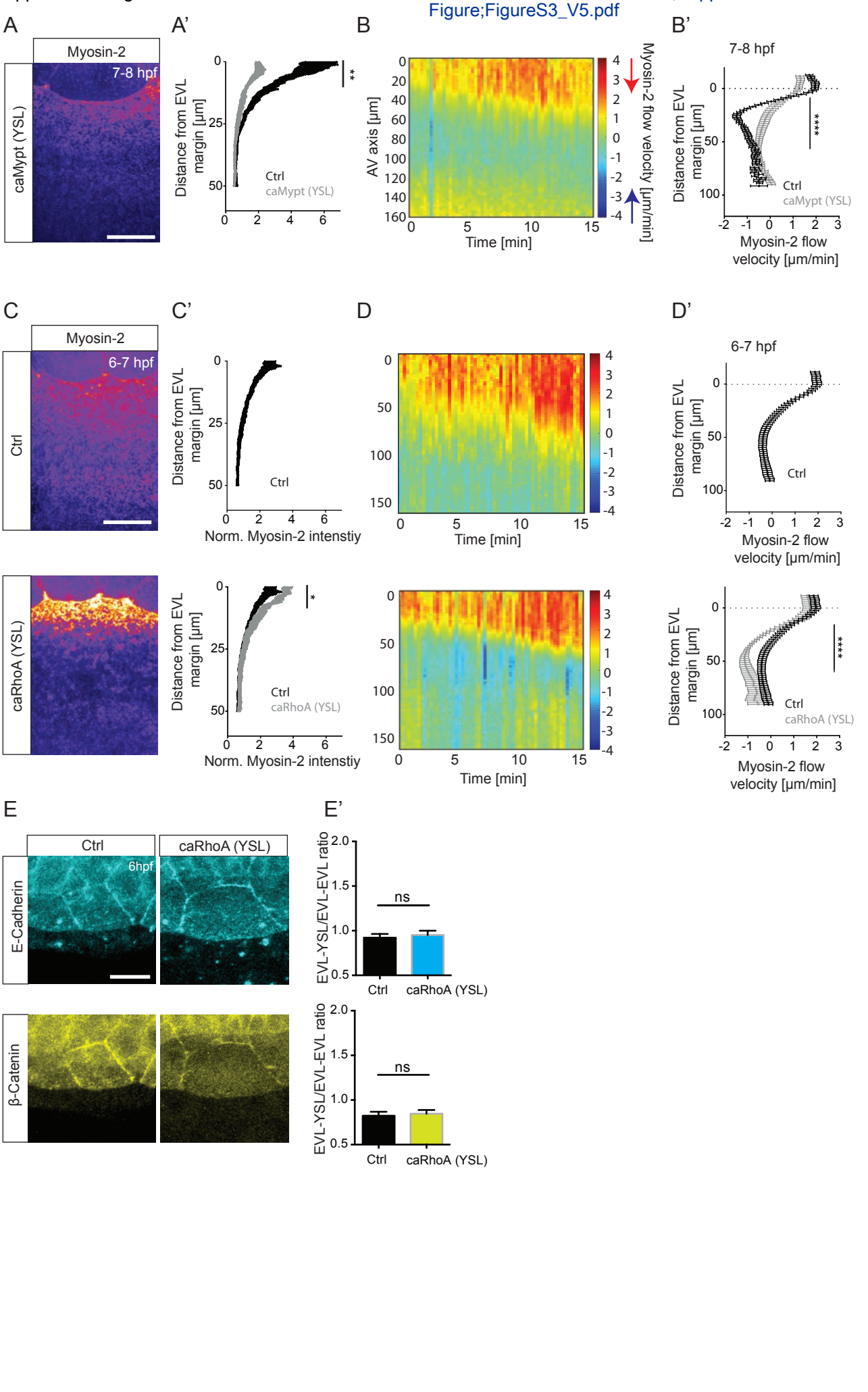

Supplemental Figure 4

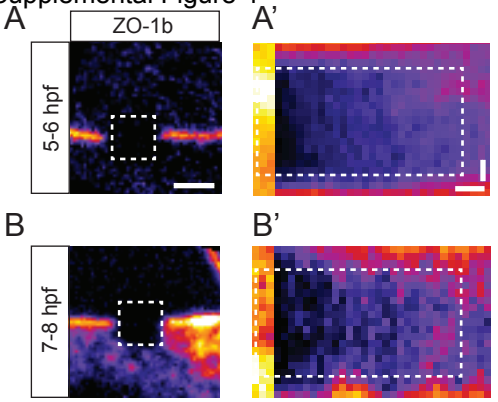

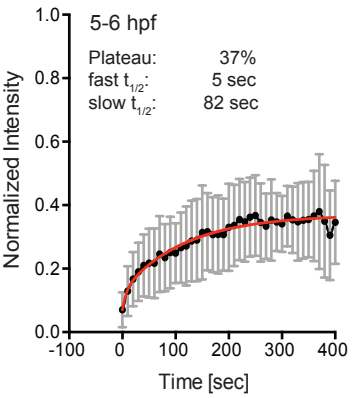

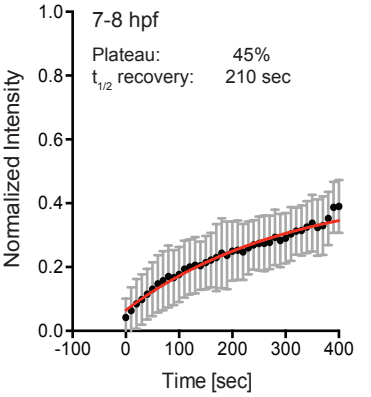

Supplemental Figure 5

Click here to access/download;Supplemental Figure;FigureS5_V2.pdf

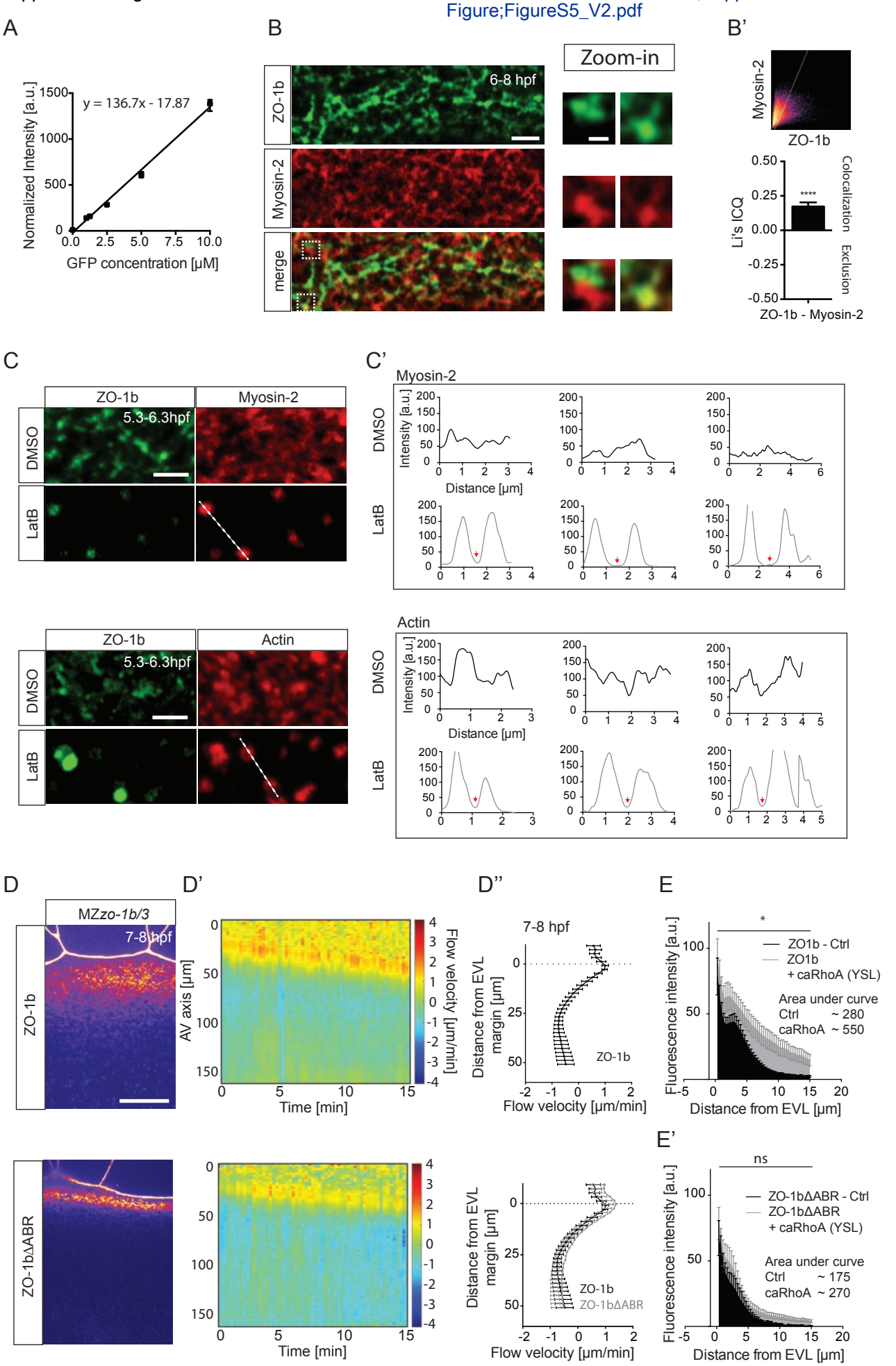

Supplemental Figure 6

Click here to access/download;Supplemental Figure;FigureS6_V1.pdf